Chemical Geology 280 (2011) 384–398

Contents lists available at ScienceDirect

Chemical Geology

journal homepage: www.elsevier.com/locate/chemgeo

Mineral–fluid partitioning of lithium and implications for slab–mantle interaction

N. Caciagli [a,*], J.M. Brenan [a], W.F. McDonough [b], D. Phinney [c]

[a] Department of Geology, University of Toronto, 22 Russell St., Toronto, ON, Canada M5S 3B1
[b] Department of Geology, University of Maryland, College Park, MD 20742, USA
[c] Lawrence Livermore National Laboratory, 7000 East Ave., Livermore, CA 94551, USA

ARTICLE INFO

Article history:
Received 18 May 2010
Received in revised form 24 November 2010
Accepted 25 November 2010
Available online 2 December 2010

Editor: D.B. Dingwell

Keywords:
Lithium
Clinopyroxene
Olivine
Plagioclase
Partitioning
Isotopic fractionation

ABSTRACT

Measurements of the partitioning of lithium between clinopyroxene, olivine, plagioclase and hydrous fluid at 800–1100 °C and 1 GPa indicate this element is mildly incompatible in the solid relative to the fluid phase, similar to mineral–melt systems. Both clinopyroxene- and olivine-fluid partitioning decrease with increasing temperature (T, K) by the relations:

$$\ln D_{Li}^{cpx/fluid} = -7.3(\pm 0.5) + (7.0(\pm 0.7) * 1000/T) \text{ and}$$
$$\ln D_{Li}^{ol/fluid} = -6(\pm 2) + (6(\pm 2) * 1000/T).$$

The lithium partition coefficients increase with pyroxene Al_2O_3 content and olivine FeO content, and decrease with plagioclase An content. Isotopic fractionation between clinopyroxene and fluid, $\Delta Li_{cpx-fluid}$, between 900 and 1100 °C ranges from −0.3 to −3.5‰ (±1.4‰).
Quantitative modeling of the evolution of lithium concentration and isotopic composition in slab-derived fluids during transport to the arc melt source indicate that fluids migrating by porous flow rapidly exchange lithium with the mantle, effectively buffering the fluid composition close to ambient mantle values, and rapidly attenuating the slab lithium signature. Fluid transport mechanisms involving fracture flow would be required to propagate a slab-like lithium signature (both elemental and isotopic) from the slab to the melt source of island arc basalts.

1. Introduction

Earth's mantle is estimated to contain ~1.5 ppm lithium with an average δ^7Li of +4‰ (McDonough and Sun, 1995; Magna et al., 2006). Lithium is mildly incompatible during partial melting, with unaltered mid-ocean ridge basalts (MORB) having lithium contents of ~5 ppm, and δ^7Li ranging from +1.5‰ to +5.6‰ with a mean value of +3.7‰ (Tomascak et al., 2008; Chan et al., 1992). Subsequent hydrothermal alteration of this material significantly increases lithium abundances (typically ranging from ~10 to 20 ppm; Bouman et al., 2004) and δ^7Li ranging from +1.7‰ to +11.8‰ (Bouman et al., 2004). The sediments deposited on the oceanic crust will reflect the composition of their source and have been subdivided into four types: pelagic clays/ooze-rich material which have lithium contents that range from ~5 to ~75 ppm and δ^7Li ranging from +1.3‰ to +14.5‰; volcanogenic sediments with ~14 ppm lithium and δ^7Li of ~+6‰; terrigenous sediments with lithium contents up to ~75 ppm and δ^7Li ranging from −1.7‰ to +2.5‰, carbonate sediments (Bouman et al., 2004). Thus, the lithium inventory in the package of material returned to the mantle by subduction bears the signature of several geochemically distinct near-surface reservoirs, making this element a potentially powerful tracer for surface inputs to the mantle and arc magmas.

Observations from the Izu arc show that the highest lithium abundances and ^{7}Li enrichment occurs in lavas at the arc front with values decreasing rapidly in samples from behind the front (Moriguti and Nakamura, 1998). This has been interpreted to indicate a diminishing contribution to the melt source by fluids derived from the downgoing slab. In contrast, lava suites from other convergent margins (e.g., Central America, Aleutians, and other Kurile suites) show evidence for large fluid inputs, but lack lithium enrichments, and have MORB-like δ^7Li (Tomascak et al., 2000, 2002; Chan et al., 2002; Walker et al., 2009). Modeling slab inputs to arc melt regions based on examination of orogenic eclogites (Marschall et al., 2007; Zack et al., 2003) or ultramafic serpentinites (Scambelluri et al., 2004) has been the focus of much work, also with contradictory conclusions. The origin of the extremely light δ^7Li contents measured in many orogenic eclogites (δ^7Li<0 to −11‰) has been attributed to either Rayleigh distillation during slab dehydration resulting in a light lithium reservoir at depth (as proposed by Zack et al., 2003), or kinetic fractionation due to diffusive influx from the host rocks during exhumation (Marschall et al., 2007) in which case the subducted slab remains a reservoir of heavy lithium at depth. The extent of lithium

* Corresponding author.
E-mail address: ncaciagli@mac.com (N. Caciagli).

0009-2541/$ – see front matter © 2010 Elsevier B.V. All rights reserved.
doi:10.1016/j.chemgeo.2010.11.025

elemental and isotopic fractionation during slab dehydration, and subsequent fluid transport through the overlying mantle is required to quantify the lithium cycle at convergent margins and fully understand the implications of the lithium contents of arc lavas. Past experimental work has focused on lithium release during slab devolatilization, in which partitioning between fluid and clinopyroxene (Brenan et al., 1998b), staurolite and mica (Wunder et al., 2007), and bulk eclogite (Kessel et al., 2005) has been determined. Fractionation of lithium isotopes has been demonstrated in fluid partitioning experiments, where enrichment of ^{7}Li occurs in fluids relative to Li-pyroxene (spodumene) at 500–900 °C and 2.0 GPa (Wunder et al., 2006), and between seawater and basalts at 25 °C to 250 °C (Millot et al., 2009) and 350 °C (Seyfried et al., 1998). Despite this work, it is still not possible to evaluate the effect of the mantle wedge on the fidelity of the slab-derived lithium signal, as data for olivine-fluid partitioning at higher temperatures and pressures are lacking. Moreover, it has not been confirmed that the enrichment of ^{7}Li in fluid relative to pyroxene applies to Li-poor, calcic compositions. This study extends the existing experimental database with new measurements of the partitioning of lithium between aqueous fluids and clinopyroxene, olivine and plagioclase at pressures and temperatures corresponding to lower crustal and upper mantle conditions (800 °C to 1200 °C; 1 GPa). Additional experiments were done to measure clinopyroxene-fluid and olivine–clinopyroxene isotopic fractionation at similar conditions. These new data are used to model the effect of the mantle wedge on the slab derived lithium signal, illuminating the behavior of lithium as an indicator of the fluid transport process.

2. Methods

Starting materials were natural single crystals of: olivine (Fo_{90}) from San Carlos, Arizona; plagioclase (bytownite; An_{76}) from Crystal Bay, Minnesota; clinopyroxene (diopside; $En_{48}Fs_1Wo_{51}$) from Dekalb, New York; and plagioclase (albite; Ab_{99}) from Mont St. Hilaire, Quebec. Table 1 gives the composition of the starting materials. In all cases, the mineral samples were first crushed to a grain size between 1 and 3 mm, after which grains free of inclusions and alteration were hand picked and cleaned in dilute HNO_3 and rinsed with ultra-pure water in an ultrasonic cleaner. For the olivine and plagioclase experiments the minerals were ground to a fine powder under ethanol with an additional $SiO_2 + Al_2O_3$ (1:1) mixture (~3 wt.% of total) added to buffer the Si and Al content of the fluid and limit olivine and plagioclase solubility (Brenan et al., 1998b; Holloway, 1971). Experiments containing olivine were not buffered for Fe loss to the Pt capsule; therefore, run product compositions are shifted to more magnesium rich compositions (from Fo_{90} to Fo_{97-99}). Experiments with bytownite as a starting mineral composition were not buffered for Na_2O loss to the fluid and as a result run product compositions are shifted from bytownite (An_{75}) to anorthite (An_{98-99}). A few plagioclase experiments contained additional albite to stabilize more sodic compositions. With one exception all experiments with Dekalb diopside as starting material had ~3 wt.% SiO_2 added (no Al_2O_3) since clinopyroxene dissolution buffers the aluminum content of the fluid. To minimize compositional zoning, a large fluid to solid ratio (4:1 by mass) was utilized for all experiments. One clinopyroxene experiment was carried out with the addition of 3 wt.% albite (+3 wt.% SiO_2) to encourage compositional zoning with respect to the aluminum concentration.

A series of mineral pair experiments were run with clinopyroxene and olivine to constrain their inter-mineral isotopic fractionation. These experiments used the same starting materials prepared as above and mixed 80:20 clinopyroxene-olivine by mass.

Isotopically labeled solutions were made from ultra pure water with lithium added as either Li_2CO_3 (LSVEC, SRM#8545) or some combination of LSVEC and a ^{6}Li spike. Solution A contained 243 ppm Li with $\delta^{7}Li = 0‰$, solution B contained 96 ppm Li with $\delta^{7}Li = -3‰$, solution C contained 306 ppm Li with $\delta^{7}Li = -88‰$, and solution D contained 180 ppm Li with $\delta^{7}Li = -46‰$. For each experiment a sample of either clinopyroxene, olivine or plagioclase powder ($\pm SiO_2$, Al_2O_3 or albite) and lithium bearing solution were added to a large volume Ni (or other metal depending on the fO_2 of the experiment) capsule with a Pt insert (Ayers et al., 1992). The oxygen fugacity generated by the Ni-lined Pt capsule is assumed to correspond to the nickel–nickel oxide buffer, which is log $fO_2 = -10.0$ ($\Delta FMQ = -0.4$; O'Neill, 1987a,b) at the experiment conditions. Similarly, the Pt lined Mo capsule is assumed to buffer the sample at the molybdenum–molybdenum oxide buffer, corresponding to log fO_2 of −14.0 at the experiment conditions ($\Delta FMQ - 4.4$; O'Neill, 1986, 1987a), and the Pt lined Re capsule is assumed to buffer the sample at the rhenium–rhenium oxide buffer corresponding to log fO_2 of −7.6 at the experiment conditions ($\Delta FMQ + 2.0$; O'Neill, 1987a; Pownceby and O'Neill, 1994). To promote crystal dissolution and re-precipitation, the bottom of the capsule was centered in the hotspot of the furnace. The temperature gradient over the length of the capsule is estimated to be less than 10 °C (Ayers et al., 1992).

The experiments were conducted in an end-loaded piston–cylinder apparatus (Boyd and England, 1960) using a 1.9 cm bore pressure vessel, employing a cylindrical graphite heater and pressure cells consisting of crushable MgO, Pyrex and NaCl. Samples were initially cold pressurized to ~0.5 GPa and then heated to 300 °C to generate sufficient internal pressure to prevent capsule deformation (Brenan et al., 1995). Temperature and pressure were then increased simultaneously with the maximum pressure being achieved by the time the sample reached 600 °C. Temperature was monitored with W26% Re–W5% Re thermocouples uncorrected for the effect of pressure on EMF. Experiments were run for 72 to 144 h and quenched by cutting power to the sample heater which resulted in temperatures dropping to <300 °C in 20 s. The capsules were then recovered, punctured and dried. Fluid masses determined by weight loss were usually >70% of the initial fluid mass; however, during the course of the experiment the capsule material became work hardened; consequently, an undetermined amount of capsule material was sheared off during puncturing. As a result, the fluid masses used in the mass balance calculations are the initial fluid masses. In the case where a watertight seal was not maintained throughout an experiment, a drop in pressure and a collapsed capsule would result.

One additional experiment was carried out in a cold seal vessel at 0.2 GPa and 800 °C. In this case the sample powder and lithium solution were loaded into a 5 mm O.D. Au capsule. The capsule was then crimped, weighed, sealed by arc welding and reweighed to check

Table 1
Composition of starting material.

	Dekalb diopside	San Carlos olivine	Crystal Bay bytownite	Mt St. Hillaire albite
SiO_2	54.77 (0.80)[a]	40.95 (0.02)	49.16 (0.20)	67.88 (0.26)
Al_2O_3	0.66 (0.100)	*<0.01*	32.67 (0.26)	19.61 (0.20)
FeO	0.85 (0.08)	9.31 (0.05)	0.50 (0.06)	*<0.03*
MgO	17.31 (0.22)	49.19 (0.42)	0.13 (0.04)	*<0.02*
CaO	25.17 (0.26)	*<0.02*	15.09 (0.28)	*<0.02*
Na_2O	0.43 (0.08)	*<0.02*	2.65 (0.12)	11.18 (0.46)
MnO	0.05 (0.06)	0.12 (0.02)	*<0.03*	*<0.03*
NiO	*<0.03*	0.39 (0.03)	*<0.03*	*<0.03*
Total	99.29	100.86	100.27	98.75
n	11	3	8	4
Li ppm[b]	9(1)	3 (1)	1.7 (0.1)	*<0.14*
δ^{7}Li(‰)	10(1)[c]	3.64 (0.15)[d]		

[a] Numbers in parentheses represent 2 sigma of the mean of n analyses.
[b] Analyzed by LA-ICPMS, numbers in parentheses represent 2 sigma of the mean of 5 analyses for diopside, 9 analyses for olivine and 2 analyses for feldspars.
[c] Analyzed by MCICP-MS, numbers in parentheses represent 2 sigma of the uncertainty on the measurement.
[d] Magna et al. (2006).

for fluid loss. The sample was loaded into a vertically mounted pressure vessel, first pressured to 0.2 GPa and then externally heated. Temperatures were monitored with an internal type K thermocouple. This experiment was quenched by removing the furnace and cooling the pressure vessel with compressed air, which resulted in temperatures dropping to <300 °C in ~3 min. Table 2 provides a summary of experimental conditions.

3. Analytical techniques

3.1. Major element analyses

Samples of starting material and splits of run products were mounted in epoxy, ground, polished with 0.3 μm grit and carbon coated. The major element compositions of the starting materials and run product clinopyroxene, olivine and plagioclase were then obtained using the Cameca SX50 Electron Probe X-ray Microanalyzer (EPMA) at the University of Toronto. An accelerating voltage of 15 kV and a focused 20 nA beam was used for all samples. The standards were albite for Na, anorthite for Al, diopside for Ca, Mg, Si, basalt for Fe, and bustamite for Mn. X-ray intensities were converted to concentrations using modified ZAF or Phi-Rho-Z correction schemes. The reported errors are the 1σ variations of (n) analyses.

3.2. MC-ICPMS

Bulk lithium isotopic composition and element concentrations were determined for run product clinopyroxene using a Multi-Collector Inductively Coupled Plasma Mass Spectrometer (MC-ICPMS) at the University of Maryland. Samples were first rinsed in ultra-pure water to remove any water-soluble Li-bearing residue and then analyzed following the method described in Teng et al. (2004). The samples, 4–10 mg of run-product clinopyroxene, were digested in a mixture of HF and HNO_3 and dissolved in a 4 M HCl solution. The lithium from the samples was then separated from the dissolved matrix by thrice processing the solutions in cation exchange columns. Samples were then introduced to the Nu-Plasma MC-ICP-MS in a 2% HNO_3 solution, and isotopic compositions were obtained by measurement of ^{7}Li and ^{6}Li simultaneously on high and low mass Faraday cups. Each sample analysis was bracketed by measurement of the NIST SRM-8545 standard. The isotopic values are reported here as δ^7Li with respect to this standard. The 2σ precision of each analysis is ±1‰. Table 3 lists measurements of standards and reference materials.

3.3. SIMS

In situ analyses of the lithium abundance and isotopic composition of the starting materials, run product clinopyroxene, olivine, and plagioclase were obtained using the Cameca IMS 3f ion microprobe at Lawrence Livermore National Laboratory. Secondary ions were generated by bombardment with a 5 to12 nA negatively charged ^{16}O primary beam, accelerated through −12.5 kV and focused to ~20 μm. The positive secondary ions were accelerated through 4.5 kV. ^{6}Li and ^{7}Li were measured with a mass resolving power of 1011, and no energy offset was applied. Background (mass 5.8), ^{6}Li and ^{7}Li were

Table 2
Summary of experimental details.

Sample	P (GPa)	T (°C)	*t (hours)*	Capsule	Starting material[a]	Solid (mg)	+ wt% SiO_2	+ wt% Ab	+ wt% Al_2O_3	Fluid (mg)	Fluid[b]	Run products
NCDL2-2	1	800	139	Pt	DD	10.66	3.9	–	–	57.09	A	Clear cpx + orange cpx
NCDL4	1	1000	67	Pt	DD	9.67	3.9	–	–	49.46	A	Clear cpx + orange cpx
NCDL5	1	1100	72	Pt	DD	10.27	3.9	–	–	36.02	A	Clear cpx
NCDL6	1	900	72	Pt	DD	6.65	3.9	–	–	36.62	A	Clear cpx + orange cpx
NCDLR	1	800	69	Pt	NCDL1	9.20	–	–	–	21.35	B	Fine grained clear cpx + ? Small xtls + quench
DiAb10	1	800	66	Pt	DD	6.82	–	9.5	–	42.01	A	Clear cpx + orange cpx
NCOL1	1	1000	72	Pt	SCO	5.27	3.3	–	3.2	42.04	A	Clear olivine + pink/red/black oxides
NCOL2	1	900	68	Pt	SCO	10.87	3.3	–	3.2	50.48	A	Clear olivine + pink/red/black oxides
NCOL3	1	1100	70	Pt	SCO	7.83	3.3	–	3.2	37.21	A	Clear olivine
LSCO8	1	1200	72	Pt	SCO	12.63	3.3	–	3.2	57.92	C	Clear olivine
NCOLR	1	800	67	Pt	NCOL2	5.03	–	–	–	35.48	B	Clear olivine + ? Mg phase + pink/red/black oxides
OlAb5	1	900	66	Pt	SCO	5.12	–	4.5	–	40.42	A	Clear olivine
NCA1	1	1000	77	Pt	CBBy	11.31	3.1	–	2.6	45.28	A	Melt + large clear anorthite
NCA2	1	900	69	Pt	CBBy	7.95	3.1	–	2.6	45.55	A	Clear anorthite
NCA3	1	800	70	Pt	CBBy	18.36	3.1	–	2.6	46.20	A	Asicular green xtls (amphibole?) + clear anorthite
NCA5	1	800	48	Pt	CBBy	9.34	3.1	–	2.6	28.69	A	Asicular green xtls (amphibole?) + clear anorthite
NCAR	1	800	72	Pt	NCA3	5.92	–	–	–	34.15	B	Zoesite
AnAb10	1	800	68	Pt	CBBy	5.49	–	12.6	–	46.36	A	Melt/quench + clear anorthite
AnAb20	1	800	55	Pt	CBBy	7.68	–	19.3	–	40.93	A	Melt/quench + clear anorthite
2m-hi[d]	1	1000	48	Pt + Re	DD + SCO[c]	6.60	–	–	–	25.45	A	Melt/quench + clear enstatite
2m-lo[e]	1	1000	48	Pt + Mo	DD + SCO[c]	5.73	–	–	–	29.66	A	Blue/grey cpx and ol + black oxides + camo oxide
Yb-1[f]	1	1000	72	Pt	DD + SCO[c]	4.80	–	–	–	30.19	A	Clear cpx and ol + black oxides
2m-1	1	900	72	Pt	DD + SCO[c]	5.33	–	–	–	40.34	A	Clear cpx + orange cpx, ol absent
2m-2	1	800	68	Pt	DD + SCO[c]	9.04	–	–	–	48.01	A	Clear olivine + clear cpx + orange cpx
2m-3	1	1000	72	Pt	DD + SCO[c]	8.47	–	–	–	47.01	A	Clear olivine + clear cpx
2m-R	1	800	72	Pt	2m-2	5.57	–	–	–	39.63	B	Clear ol + cpx + monticellite + black oxides
LDi-10[g]	1	900	142	Pt	DD	16.3	3.9	–	–	86.7	C	Clear cpx + orange cpx
LDi-11[g]	1	900	72	Pt	DD	5.1	3.9	–	–	52.4	C	Clear cpx + orange cpx
LDi-12[g]	1	900	68	Pt	LDi-10	4.89	13	–	–	66.35	D	Clear cpx + orange cpx
LDi-15	1	900	75	Pt	DD	6.86	3.9	–	–	63.63	C	Clear cpx
LDi-17	1	1000	20	Pt	DD	9.25	3.9	–	–	59.82	C	Clear cpx + black oxides
LDi-18	1	1100	70	Pt	DD	9.66	3.9	–	–	31.13	C	Clear cpx

[a] DD: Dekalb diopside, SCO: San Carlos olivine, CBBy: Crystal Bay bytownite.
[b] Fluid compositions; A: 243 ppm Li, B: 96 ppm Li, C: 306 ppm Li, D: 180 ppm Li.
[c] 82 wt.% DD + 18 wt.% SCO.
[d] Capsule materials result in log fO_2 of −5.
[e] Capsule materials result in log fO_2 of −15.
[f] 0.25 mg of Yb_2O_3 added.
[g] Ti outer capsule.

Table 3
Standards and reference materials.

	Li (ppm)[a]	Reference
International standards		
NBS 612	41.54 (2.87)	Pearce et al. (1997)
NBS 612	42 (2)	This study[b], LA-ICPMS
NBS 610	484.6 (21.7)	Pearce et al. (1997)
NBS 610	489 (40)	This study[c], LA-ICPMS
JG1a	79.5 (4.5)	Imai et al. (1995)
JG1a	92 (6)	This study, LA-ICPMS
JB-2	7.78 (1.39)	Imai et al. (1995)
JB-2	8 (1)	This study, LA-ICPMS
BCA1	13.3	Ryan and Langmuir (1987)
BCA1	12 (1)	This study, LA-ICPMS
JGB-1	4.59 (.90)	Imai et al. (1995)
JGB-1	5 (1)	This study, LA-ICPMS
In house standards		
San Carlos olivine	3 (1)	This study, LA-ICPMS
San Carlos olivine	1.6 (0.08)	Magna et al. (2006), SIMS
Dekalb diopside	9 (1)	This study, LA-ICPMS
Dekalb diopside	7 (2)	This study, MC-ICPMS
Kunlun diopside	42 (3)	This study, LA-ICPMS
	δ^7Li(‰)	Reference
International standards		
IRMM016	+0.1 (1)	This study, MC-ICPMS
IRMM016	−0.1 (1)	Teng et al. (2004)
IRMM016	+0.13 (1)	Jeffcoate et al. (2004)
In house standards		
UMD-1	+55 (1)	This study, MC-ICPMS
UMD-1	+55 (1)	Teng et al. (2004)
San Carlos olivine	+3.64 (0.2)	Magna et al. (2006), SIMS
San Carlos olivine	+1 (4)	This study, SIMS corrected[d]
Dekalb diopside	+9 (4)	This study, SIMS corrected[d]
Dekalb diopside	+10 (1)	This study, MCICPMS

[a] Numbers in parentheses represent 2 sigma errors.
[b] Analyzed using NIST 610 as standard unless otherwise noted.
[c] Analyzed using NIST 612 as standard.
[d] Values are corrected for instrument mass fractionation (see text).

counted on an electron multiplier for 2 s, 10 s and 2 s respectively over 120 to 400 counting cycles, depending on count rate. Fig. 1 shows the 'uncorrected' δ^7Li values of the internal reference materials measured by SIMS plotted against the δ^7Li values measured by MC-ICP-MS. Internal reference materials used were Dekalb diopside (measured in this study by MC-ICP-MS), San Carlos olivine (value from Magna et al., 2006), and clinopyroxene from experiment NCDL6 (measured in this study by MC-ICP-MS). The δ^7Li values of the internal reference materials measured by MC-ICP-MS range from −3‰ to +10‰ whereas the corresponding 'uncorrected' δ^7Li values measured by SIMS range from +15‰ to +30‰. The discrepancy between the SIMS and MC-ICP-MS values is due to instrument- and matrix-derived mass fractionations that result during ion microprobe analyses (Decitre et al., 2002; Deloule et al., 1992). It is important to note that all the values plot on a single line with a slope of ~1 (0.8 ± 0.4, $r^2 = 0.95$), demonstrating the absence of any matrix effect on the instrumental fractionation. The ^{7}Li/^{6}Li ratios in all phases can therefore be corrected for instrumental fractionation using a single instrumental correction factor, Δi (Decitre et al., 2002):

$$\Delta i = \delta^7 Li_{SIMS} - \delta^7 Li_{MC-ICPMS}. \quad (1)$$

The ^{7}Li/^{6}Li ratio of Dekalb diopside was used as the internal reference material to determine Δi, which was found to be −20‰ for the single analytical session during which the reported isotopic compositions were determined. Applying this factor to the $\delta^7 Li_{SIMS}$ for San Carlos olivine and the NCDL6 experiment diopside brings their δ^7Li values to within error of that determined by MC-ICPMS. Because the concentration of lithium in Dekalb diopside is greater than that of

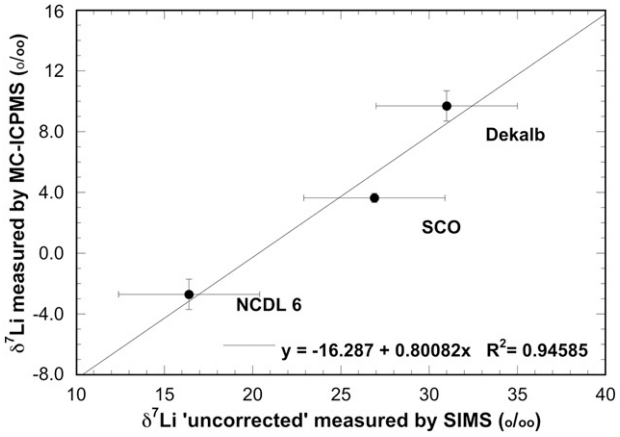

Fig. 1. Internal reference materials. Plot of δ^7Li values measured by MC-ICPMS versus uncorrected δ^7Li values measured by SIMS of the internal reference materials, Dekalb diopside and San Carlos olivine, as well as the run product from one experiment (NCDL6). The δ^7Li values measured by MC-ICPMS for Dekalb diopside and NCDL6 are from this study and SCO is measured by MC-ICPMS from Magna et al. (2006). Error bars for 'uncorrected' SIMS δ^7Li are 2σ, based on counting statistics. The error bars for δ^7Li measured by MC-ICPMS are ± 1‰ (2σ) or the published 2σ errors (± 0.3‰; Magna et al., 2006). Note that the discrepancy between values is due to instrument mass fractionation (Decitre et al., 2002). All values plot on a single line with a slope of ~1 (0.8 ± 0.4) suggesting the absence of any significant matrix effect on the lithium instrumental isotopic fractionation (see text).

San Carlos olivine (i.e. 8.6 ppm and 67 ppm vs. 2.5 ppm), the Dekalb diopside was primarily used as an internal reference material for all analyses.

3.4. LA-ICPMS

Lithium abundances in clinopyroxene, olivine, and plagioclase were determined *in situ* by laser ablation inductively coupled plasma mass spectrometry (LA-ICP-MS) at the University of Toronto. The system employs a frequency quintupled Nd:YAG laser operating at 213 nm, coupled to a VG PQExcell quadrupole ICP-MS with He

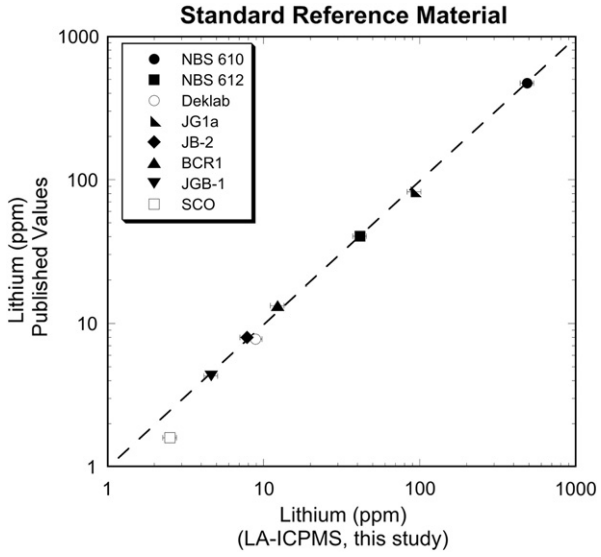

Fig. 2. Standards and reference material. Lithium abundance of various standard reference materials (values taken from literature; see text) and internal reference material (SCO and Dekalb; measured by MC-ICPMS) plotted against lithium abundance determined in this study by LA-ICP-MS. NBS 610 was used as the standard reference material (SRM) for all analyses. The value for NBS 610 was determined using NBS 612 as the SRM. Error bars for lithium concentrations from this study are 2σ, based on standard deviation of replicate measurements (typically 5 or more analyses for each).

flushing the ablation cell to enhance sensitivity (Eggins et al., 1998). Conditions for laser ablation of the phases analyzed in this study were a laser repetition rate of 10 Hz, and a 50–75 μm spot size. Analyses were collected in blocks of 20, with the first and last four spectra acquired on standard reference materials (SRM). Factory-supplied time resolved software was utilized for the acquisition of individual analyses. A typical analysis involved 20 s of background acquisition with the ablation cell being flushed with He, followed by laser ablation for 60 s, then at least 60 s of washout. Data reduction was done off-line using the GLITTER version 5.3 software package, supplied by Macquarie Research, Ltd. Prior to each analytical session, torch position and quadrupole settings were tuned to maximize the signal at mass 7. Ablation yields in the unknowns were corrected by referencing to the known concentration of ^{43}Ca or ^{55}Mn as determined previously by electron microprobe analyses. Lithium concentrations were quantified using the "in house" standard Kunlun diopside, which contains 42 ± 2 ppm lithium. This standard was used routinely because it generated a lower lithium background over the course of the analytical session compared to that produced by NIST 610. Kunlun diopside was, in turn, characterized using NIST 610 silicate glass, which contains 484 ± 21 ppm lithium (Pearce et al., 1997). The precision for concentration measurements is better than 10% based on counting statistics. As a further check on the accuracy of the analytical method glasses made from powders of various rock reference materials were analyzed. Glasses were prepared by fusing approximately 50 mg of powder in sealed platinum capsules at 1 GPa and 1600 °C for 5 min. Reference glasses were quantified using NIST 610 as the standard, and values are provided in Table 3. Fig. 2 shows the 1:1 correlation between the published values for Li abundances with those measured by LA-ICPMS in this study.

4. Results

4.1. Major element chemistry

Fig. 3 shows the size and morphology of run product clinopyroxene, olivine and plagioclase. The run products display considerable coarsening compared to starting materials, and well-developed crystal faces. Crystals grew as aggregates of grains nucleating on the lid and/or upper walls of the capsule. Table 4 lists the major element composition of the clinopyroxene, olivine and plagioclase run products produced in this study. The minimum detection limits are

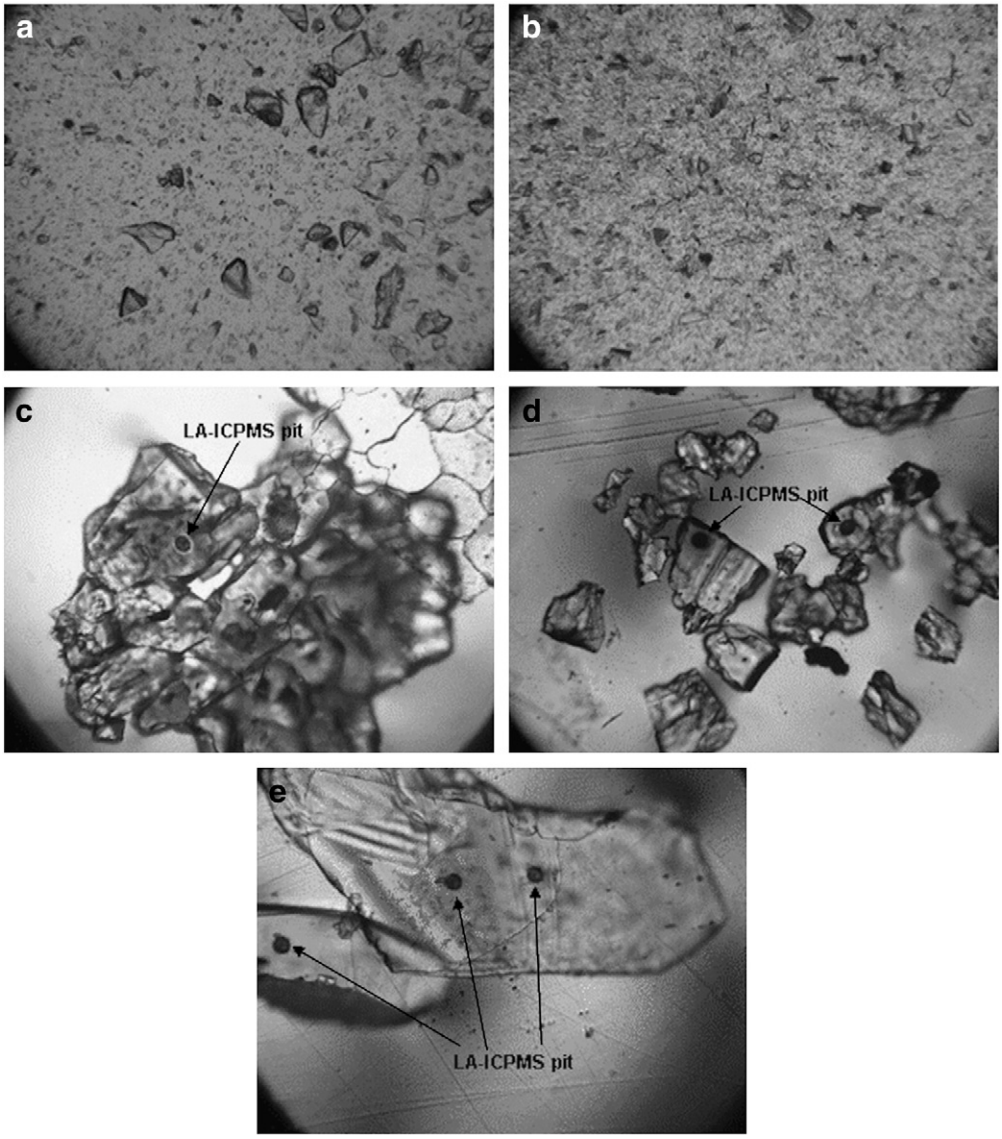

Fig. 3. Photomicrographs of starting material and run products. (a) Starting material San Carlos olivine mounted in oil, (b) starting material Dekalb diopside mounted in oil, (c) run product olivine from NCOL3 mounted in epoxy, (d) run product diopside from NCDL 4 mounted in epoxy and (e) NCAL 2 mounted in epoxy. LA-ICPMS pits in run product crystals are 50 μm in diameter. All photomicrographs are taken in plane polarized light at 100× magnification.

Table 4
Run product major element composition.

Sample	SiO_2	Al_2O_3	FeO	MnO	MgO	CaO	Na_2O	NiO	Total	*n*	ppm Yb	Di%	Jd%	Tsc%	Fo%	An%
Single phase exp																
Clinopyroxene																
NCDL2-2	54.72 (0.29)	0.22 (0.10)	0.57 (0.21)	0.06 (0.03)	18.26 (0.17)	25.26 (0.26)	0.02 (0.01)	nd	99.11	16		97	0	1		
NCDL4	54.84 (0.30)	0.23 (0.06)	0.43 (0.18)	0.05 (0.03)	17.98 (0.16)	25.82 (0.13)	0.02 (0.02)	nd	99.37	14		99	0	1		
NCDL5	55.02 (0.30)	0.21 (0.06)	0.05 (0.09)	0.03 (0.02)	18.36 (0.16)	25.77 (0.24)	0.02 (0.01)	nd	99.46	11		100	0	0		
NCDL6	54.77 (0.23)	0.32 (0.11)	0.78 (0.27)	0.05 (0.01)	17.87 (0.18)	25.38 (0.12)	nd	nd	99.17	5		95	1	1		
NCDLR	54.99 (0.23)	0.47 (0.13)	0.76 (0.23)	0.05 (0.03)	17.48 (0.26)	25.41 (0.24)	0.27 (0.17)	0.11 (0.16)	99.54	14		96	2	0		
DiAb10	54.59 (0.43)	0.32 (0.09)	1.79 (0.44)	0.04 (0.03)	17.89 (0.27)	25.28 (0.11)	nd	0.04 (0.03)	99.95	8		96	0	2		
Olivine																
NCOL1	42.51 (0.22)	0.04 (0.01)	1.12 (0.10)	0.10 (0.04)	55.59 (0.18)	0.03 (0.01)	nd	0.32 (0.05)	99.72	9					99	
NCOL2	42.45 (0.22)	0.04 (0.01)	2.07 (0.24)	0.13 (0.03)	54.74 (0.31)	0.04 (0.01)	nd	0.33 (0.11)	99.80	9					98	
NCOL3	43.74 (0.27)	0.07 (0.01)	0.06 (0.02)	0.05 (0.03)	56.72 (0.20)	0.06 (0.01)	nd	0.03 (0.03)	100.73	9					100	
LSCO8	42.51 (0.14)	0.09 (0.02)	1.32 (0.63)	0.16 (0.10)	56.61 (0.64)	0.04 (0.00)	nd	0.31 (0.39)	101.04	7					99	
NCOR	41.81 (0.42)	0.03 (0.01)	0.12 (0.03)	0.09 (0.03)	53.55 (0.70)	0.01 (0.01)	nd	4.53 (0.70)	100.14	13					100	
OlAb5	42.62 (0.05)	0.02 (0.01)	0.83 (0.11)	0.12 (0.02)	55.73 (0.10)	0.09 (0.01)	nd	0.36 (0.02)	99.77	5					99	
Plagioclase																
NCA1	42.99 (0.14)	37.36 (0.15)	0.03 (0.03)	nd	nd	19.77 (0.14)	0.15 (0.03)	na	100.30	22						98
NCA2	43.04 (0.13)	37.19 (0.15)	0.22 (0.03)	nd	nd	19.78 (0.11)	0.15 (0.04)	na	100.38	14						99
NCA3	44.05 (0.41)	36.32 (0.31)	0.25 (0.03)	nd	nd	18.81 (0.29)	0.66 (0.17)	na	100.09	23						94
NCA5	44.57 (0.26)	35.66 (0.22)	0.06 (0.05)	0.03 (0.02)	nd	18.23 (0.22)	0.97 (0.09)	0.03 (0.02)	99.55	8						91
NCAR — zoesite	39.53 (0.44)	34.18 (0.12)	0.24 (0.13)	nd	0.55 (0.10)	24.38 (0.24)	nd	na	98.88	20						
AnAb10	43.09 (0.01)	36.66 (0.10)	0.14 (0.04)	0.02 (0.01)	0.01 (0.01)	19.23 (0.16)	0.36 (0.08)	nd	99.52	4						97
AnAb20	43.99 (0.26)	35.87 (0.24)	0.06 (0.06)	nd	0.02 (0.01)	19.15 (0.18)	0.41 (0.03)	am	99.50	10						93
NCA1 melt	43.47 (0.99)	26.14 (0.36)	0.12 (0.03)	nd	1.16 (0.06)	14.78 (0.54)	0.26 (0.05)	na	85.93	10						
NCA2 melt	60.36 (2.59)	21.64 (1.46)	0.61 (0.09)	nd	0.40 (0.10)	2.28 (0.48)	0.86 (0.31)	na	86.15	4						
Two phase exp																
2m-hi opx	59.23 (0.13)	0.14 (0.06)	1.92 (0.09)	0.05 (0.02)	38.52 (0.23)	0.09 (0.01)	nd	0.03 (0.04)	99.99	9						
2m-lo olivine	42.56 (0.41)	0.04 (0.01)	0.12 (0.10)	0.14 (0.05)	57.05 (0.60)	0.11 (0.06)	nd	0.01 (0.02)	100.03	9					100	
2m-lo cpx	56.04 (0.30)	0.53 (0.09)	nd	0.07 (0.01)	21.06 (0.49)	22.71 (0.65)	nd	nd	100.41	8		85	1	1		
Yb-1 olivine	42.60 (0.41)	0.05 (0.04)	0.25 (0.07)	0.16 (0.04)	55.47 (1.20)	1.11 (0.28)	nd	0.04 (0.02)	99.67	13	2868				100	
Yb-1 cpx	55.73 (0.22)	0.20 (0.05)	0.13 (0.06)	0.03 (0.02)	18.69 (0.16)	25.84 (0.11)	nd	0.16 (0.13)	100.78	12	1441	98	0	1		
2m-1 cpx	54.40 (0.34)	0.52 (0.11)	1.30 (0.37)	0.05 (0.03)	17.87 (0.22)	25.46 (0.26)	nd	0.03 (0.02)	99.63	6		97				
2m-2 olivine	42.67 (0.30)	0.04 (0.01)	0.02 (0.01)	0.10 (0.06)	42.67 (0.30)	0.26 (0.18)	nd	nd	85.77	4					100	
2m-2 cpx	55.30 (0.34)	0.24 (0.13)	0.36 (0.49)	0.05 (0.02)	18.40 (0.33)	25.47 (0.16)	nd	0.02 (0.02)	99.84	5		97	1	0		
2m-3 olivine	42.80 (0.14)	nd	nd	0.04 (0.02)	55.96 (0.17)	0.95 (0.04)	nd	nd	99.75	9					100	
2m-3 cpx	55.35 (0.14)	0.23 (0.04)	0.21 (0.10)	nd	18.50 (0.12)	25.59 (0.10)	nd	nd	99.87	10		98	1	0		
2m-R monticillite	38.53 (0.10)	0.03 (0.02)	0.15 (0.02)	0.12 (0.04)	26.23 (0.25)	34.66 (0.27)	nd	0.07 (0.04)	99.80	8					100	
2m-R cpx	54.80 (0.18)	0.29 (0.04)	0.93 (0.09)	0.02 (0.02)	18.04 (0.07)	25.67 (0.13)	nd	0.02 (0.02)	99.76	9		98	0	2		
2m-R olivine	42.40 (0.14)	0.04 0.02	0.35 (0.11)	0.12 (0.03)	55.55 (0.41)	0.91 (0.13)	nd	0.16 (0.05)	99.52	4					100	

Numbers in parentheses represent 2 sigma errors.

less than the lowest value cited for each element and the number in parentheses refers to 1σ of the standard deviation for *n* analyses.

4.2. Mineral–fluid lithium partitioning

Table 5 lists the lithium contents of experimentally-produced crystals as analyzed by LA-ICPMS and the calculated mineral–fluid or –melt distribution coefficients. Mineral/fluid distribution coefficients were determined by mass balance (see the Supplementary material for details). The lithium content of run product phases ranges from 5 ppm to 7 ppm for clinopyroxene, 13 ppm to 466 ppm for olivine, and 20 ppm to 70 ppm for plagioclase. Generally, the lithium mineral/fluid distribution coefficients decrease in the order: olivine (2.51–0.17), plagioclase (0.32–0.090) and clinopyroxene (0.32–0.07).

Consistent with mineral–fluid equilibrium is the relatively homogeneous distribution of lithium in run-product phases. The concentration of lithium from grain to grain within a single experiment typically vary by 14% relative to the mean concentration (i.e., just beyond counting statistics) although, in a few cases, values varied as much as 30% from grain to grain. Owing to limitations imposed by grain size, and the need for a relatively large (50 um) spot for precise analysis, most grains had "room" for only one or two analyses. Hence, within-grain homogeneity could only be assessed by monitoring the time-resolved spectra produced during laser ablation. Fig. 4 shows the time resolved spectra for ^{7}Li and ^{43}Ca measured for clinopyroxene produced in the lowest temperature partitioning experiment (800 °C). Time resolved spectra for all experiments typically display similarly constant count rates, reflecting homogeneous grains. The slight reduction in count rate with time is due to a reduction in pit diameter during ablation. Although absolute count rates decrease, the relative ^{7}Li and ^{43}Ca signals remain constant.

An additional test for mineral–fluid equilibration was attempted by measuring partition coefficients in reversal experiments where crystals previously equilibrated with solution 'A' were re-equilibrated with solution 'B,' containing a lower concentration of lithium and a differing isotopic composition. These reversal experiments confirm isotopic equilibrium, but changes in the mineral assemblage during the reversal step (e.g., zoisite in the anorthite reversal, Mg-hydroxides in the olivine reversal, monticellite in the olivine + clinopyroxene reversal, and an unidentified phase in the clinopyroxene reversal) made mass balance inaccurate, resulting in large uncertainties in the calculated $D_{Li}^{min/fluid}$. Equilibration within a short time is to be expected in these experiments given that lithium diffusion is rapid in silicates. For example, values for lithium diffusion coefficients at 800 °C (Dohmen et al., 2010; Coogan et al., 2005; Caciagli-Warman, 2010) predict a penetration distance of 150 μm into clinopyroxene and 50 μm into olivine after 72 h. This is consistent with the lithium homogeneity of similarly sized grains in experimental run products.

Table 5
Run product lithium concentration.

Sample	Li ppm	2 s[a]	*n*	Min/fluid	2 s	Ol/cpx	2 s	Min/melt	2 s
NCDL2-2	98	32	2	0.3	0.1				
NCDL4	33	14	3	0.14	0.06				
NCDL5	27	12	3	0.11	0.05				
NCDL6	62	32	2	0.3	0.1				
NCDLR	7	2	3	0.07	0.02				
DiAb10	49.9	0.6	2	0.21	0.03				
NCOL1	101	10	3	0.47	0.04				
NCOL2	124	13	4	0.57	0.06				
NCOL3	86	35	2	0.4	0.2				
LSCO8	49	12	3	0.17	0.04				
NCOLR	13	2	3	0.14	0.02				
OlAb5	279	23	3	1.34	0.02				
NCA1	21	7	3	0.09	0.03				
NCA2	21	2	2	0.09	0.02				
NCA3	39	18	2	0.17	0.08				
NCA5	70	34	3	0.3	0.2				
NCAR*-zoesite	0.3	0.4	2						
AnAb10	31	11	2	0.1	0.1				
AnAb20	50	20	4	0.21	0.08				
NCA1-melt	1120	224	1					0.02	0.01
NCA2-melt	1197	239	1					0.017	0.004
2m-1 cpx	14	3	2	0.06	0.01				
2m-2 olivine	78	7	1			1.6	0.2		
2m-2 cpx	50	4	2						
2m-3 olivine	51	11	3			4	2		
2m-3 cpx	13	7	2						
2m-R olivine	31	2	1			1.2	0.3		
2m-R cpx	26	5	1						
2m-R monticillite	39	24	2						
2m-hi enstatite	5	3	3	0.02	0.01				
2m-lo olivine	29	9	2			0.7	0.4		
2m-lo cpx	42	21	3						
Yb-1 olivine	174	15	1			10	4		
Yb-1 cpx	17	6	3						

[a] 2s refers to the standard deviation for n analyses and reflects the degree of sample heterogeneity.

4.2.1. Clinopyroxene

Most clinopyroxene-fluid partitioning experiments contained only clinopyroxene as the run-product solid, except experiment NCDL3, which produced a 1:1 mixture of olivine and clinopyroxene crystals. It seems likely that this mixed phase assemblage was produced by magnesium contamination from the ceramic pressure cell during sample assembly or loading. Electron microprobe traverses across individual clinopyroxene grains revealed a homogenous distribution of major elements. These grains have much lower Al_2O_3 (~0.5 wt.% to ~0.2 wt.%), FeO (~0.9 wt.% to ~0.4 wt.%) and Na_2O concentrations (~0.02 wt.% to ~0.30 wt.%) than is typical for equilibrated upper mantle clinopyroxene (~3–7 wt.% Al_2O_3, ~2–6 wt.% FeO, ~0.75–2.5 wt.%; Seitz and Woodland, 2000). However, the MgO contents of run-product clinopyroxenes (~17 wt.% to ~21 wt.%) are similar to those in mantle xenoliths (~14–20 wt.% MgO; Seitz and Woodland, 2000). The low FeO content of experimentally-produced clinopyroxenes are due to losses to the platinum capsule. The depletion of Al_2O_3 and Na_2O is due to strong partitioning into the aqueous fluid. Reversal experiments were attempted, but the re-equilibration of the run product material from experiment NCDL1 caused Fe and water soluble elements (i.e. Na, Ca, etc.) to become further depleted, such that the final solid composition was no longer in the stability field of diopside alone.

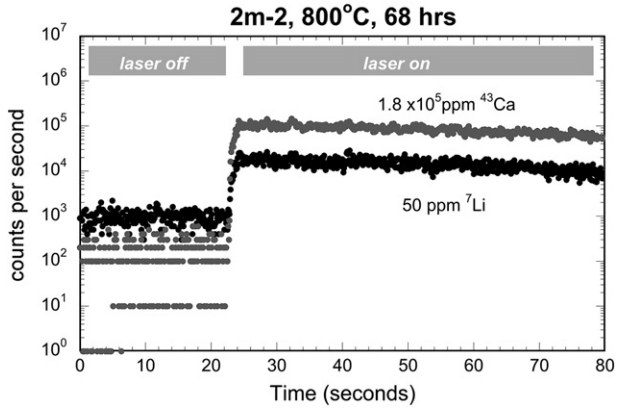

Fig. 4. Time resolved spectra. Example of time resolved spectra for an individual clinopyroxene crystal from a cpx/fluid partitioning experiment at 800 °C for 68 h. The first ~20 s of the analysis was done with the laser shutter in place for background measurements, followed by ~60 s of sample ablation. Note that the ^{7}Li signal is consistent with respect to the ^{43}Ca signal, which is an indication of homogeneity, confirming mineral–fluid equilibrium of both major and trace elements.

The range of $D_{Li}^{cpx/fluid}$ (0.07 to 0.61) measured in this study is similar to that measured by Brenan et al. (1998b; 0.08 to 0.25) and values of clinopyroxene/silicate melt partitioning measured by Brenan et al. (1998a; 0.14 to 0.27) and Blundy et al. (1998; 0.254). Lithium partitioning between clinopyroxene and fluid decreases from 0.32 to 0.09 with increasing temperature from 800 °C to 1100 °C at 1 GPa (Fig. 5). A linear regression of the data (excluding the reversal, NCDLR) yields the relationship:

$$\ln D_{Li}^{cpx/fluid} = -7.3(\pm 0.5) + 7.0(\pm 0.7) * 1000 / T \left(R^2 = 0.98\right) \quad (2)$$

where T is temperature in Kelvin.

4.2.2. Olivine

Olivine partitioning experiments occasionally produced some oxide grains and in the reversal experiment (NCOR), an unidentified magnesian phase. All are likely due to incongruent dissolution of olivine. Electron microprobe traverses of individual crystals show the

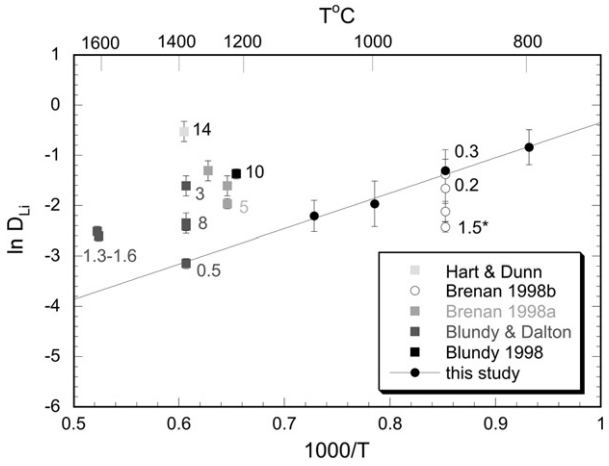

Fig. 5. ln $D_{Li}^{cpx/fluid}$ vs. 1000/T. A plot of ln $D_{Li}^{cpx/fluid}$ as a function of 1000/T for cpx/fluid partitioning measured in this study, demonstrating the temperature dependence of lithium partitioning between clinopyroxene and hydrous fluids. A linear regression of the data yields: ln $D_{Li}^{cpx/fluid} = -7.38 + 7.04 * 1000/T$ ($R^2 = 0.98$) where T is temperature in Kelvin. NCDLR (reversal) was not used in the regression (see text). Also shown are the data from the experiments of Hart and Dunn (1993), Brenan et al. (1998a,b), Blundy and Dalton (2000). The data points are labeled with the wt.% Al_2O_3 content of the run product clinopyroxene and suggest that lithium may be coupled with Al^{3+} as a substitution mechanism in clinopyroxene. Error bars for the partition coefficients measured in this study are 2σ, based on the standard deviation of *n* analyses (see Table 5).

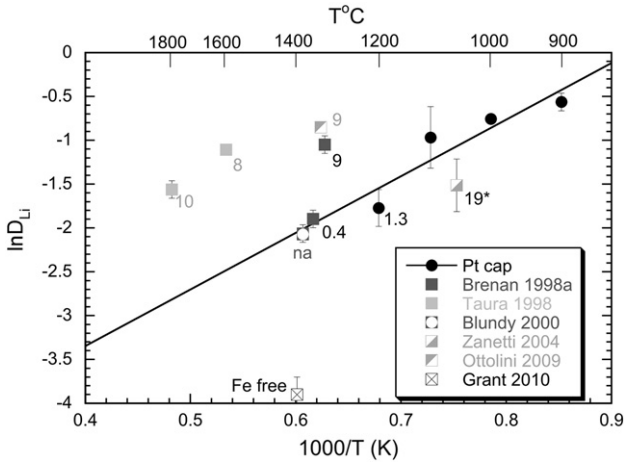

Fig. 6. ln $D_{Li}^{ol/fluid}$ vs. 1000/T. A plot of ln D_{Li} $^{ol/fluid}$ as a function of 1000/T measured in this study, demonstrating the temperature dependence of lithium partitioning between olivine and hydrous fluids. A weighted linear regression of the data (excluding the reversal, NCOLR) yields the relationship: ln $D_{Li}^{ol/fluid} = -5.93 + 6.46 * 1000/T$ ($R^2 = 0.82$) where T is temperature in Kelvin. Also shown are the experiments of Brenan et al. (1998a), Taura et al. (1998), Blundy and Dalton (2000), Zanetti et al. (2004) and Grant and Wood (2010). The data points are labeled with the wt.% FeO content of the run product olivine, and suggest that lithium couples with Fe^{3+} as an exchange mechanism in olivine. The experiment of Zanetti et al. (2004), 19*, was conducted at very reducing conditions and most likely contained less Fe^{3+} than the experiments in this study. Error bars for the partition coefficients measured in this study are 2σ, based on the standard deviation of *n* analyses (see Table 5).

run product olivines to be homogenous with respect to major element chemistry. Iron loss to the platinum capsule resulted in considerably more magnesian (Fo# 98 to 99) olivines than those naturally occurring in the mantle. Reversal experiments were attempted, but the re-equilibration of the run product material from experiment NCOL2 caused Fe and water soluble elements (i.e. Na, Ca, etc.) to become further depleted, such that the final solid composition was no longer in the stability field of olivine alone.

The range of $D_{Li}^{ol/fluid}$ (0.17–0.57) measured in this study is similar to the $D_{Li}^{ol/melt}$ measured by Brenan et al. (1998a; 0.13–0.35) and that of Ottolini et al. (2009; 0.418–0.436). The exception to this is the experiment with added albite (OlAb10) which produced a $D_{Li}^{ol/fluid}$ value of 1.34 ± 0.02. The temperature dependence of lithium partitioning between olivine and hydrous fluids can be demonstrated on a plot of ln $D_{Li}^{ol/fluid}$ versus 1000/T (Fig. 6). A linear regression of the data (excluding the reversal, NCOLR) yields the relationship:

$$\ln D_{Li}^{ol/fluid} = -6.0(\pm 2) + 6.5(\pm 2) * 1000 / T \left(R^2 = 0.82\right) \quad (3)$$

where *T* is temperature in Kelvin.

4.2.3. Plagioclase

The starting material for these experiments was bytownite (An_{76}), but run product compositions are very close to end member anorthite (An_{96-99}) due to Na-loss to the fluid. The reversal run, NCAR, which consisted of re-equilibrating material from NCA3, resulted in zoisite + unidentified Al-rich phase due to further depletion of water soluble elements (Na and Ca). At 1000 °C run products consisted of 30% melt, 70% anorthite crystals, at 900 °C the amount of melt was negligible, and runs at 800 °C were melt free. Electron microprobe traverses demonstrate these grains are homogenous with respect to major elements. In two of the experiments, AnAb10 and AnAb20, the Na content of the fluid was buffered by addition of albite. This resulted in homogenous anorthite crystals with only slightly more sodic compositions (see Table 4).

$D_{Li}^{plag/fluid}$ is 0.09 to 0.32 and is similar to the $D_{Li}^{plag/melt}$ measured by Blundy et al. (1998; 0.151 for An_{40}). The data obtained in this study show a linear relationship with a negative slope on a plot of ln $D_{Li}^{plag/fluid}$ versus X_{An} suggesting that lithium is more compatible in albite than in anorthite (Fig. 7). Linear regression of the six partitioning experiments yields the relationship, in J mol^{-1}:

$$RT\ln D_{Li}^{plag/fluid} = 162,000(\pm 26,000) - 188,000(\pm 28,000)(X_{An}) \left(R^2 = 0.96\right) \quad (4)$$

where *R* is the gas constant, *T* is temperature in Kelvin, and X_{An} is the anorthite content of the plagioclase. Following Blundy and Wood (1991), $RT\ln D_{Li}^{plag/fluid}$ is used rather than ln $D_{Li}^{plag/fluid}$ to correct for temperature in the linear regression.

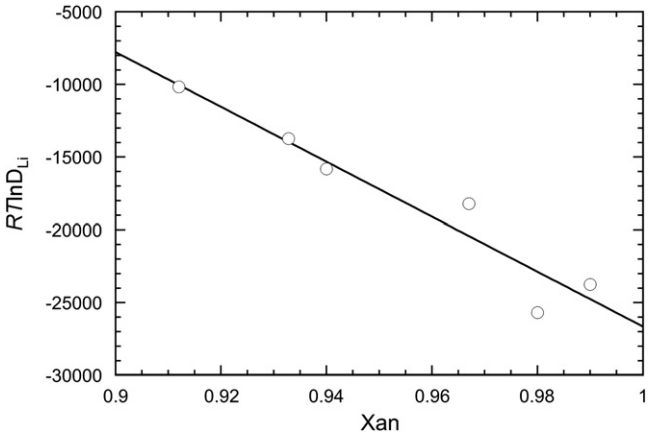

Fig. 7. Anorthite/fluid lithium partitioning. Plot of $RT\ln D_{Li}^{plag/fluid}$ as a function of the mole fraction of anorthite in plagioclase (X_{An}). Lithium partitioning between anorthite and fluid shows a linear relationship with a negative slope over the range of X_{An} from 0.91 to 0.99 indicating that lithium is more compatible in albite than in anorthite. Linear regression of the six partitioning experiments yields the relationship, in J mol^{-1}: $RT\ln D_{Li}^{plag/fluid} = 162{,}170 - 188{,}820(X_{An})$ ($R^2 = 0.96$). The primary control on lithium partitioning between plagioclase and hydrous fluids is the composition of the feldspar (see text). 2σ errors for the partition coefficients measured in this study are smaller than the symbol used, and based on the standard deviation of *n* analyses (see Table 5).

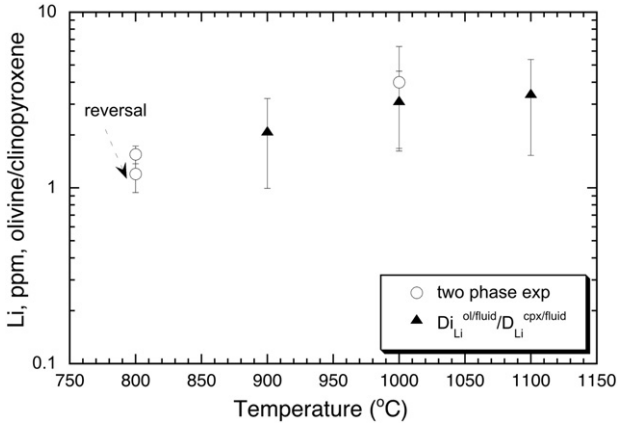

Fig. 8. Olivine/clinopyroxene lithium partitioning. $D_{Li}^{ol/cpx}$ as a function of temperature (°C) for two phase experiments (open symbols) and the ratio of $D_{Li}^{olivine/fluid}/D_{Li}^{cpx/fluid}$ calculated from single phase experiments (solid symbols). The relatively constant value of $D_{Li}^{ol/cpx}$ determined by both methods suggests that olivine/clinopyroxene partitioning of lithium is not strongly dependent on temperature. Error bars for the partition coefficients measured in this study are 2σ, based on the standard deviation of *n* analyses (see Table 5).

4.3. Olivine–clinopyroxene pair experiments

Experiments in which olivine and clinopyroxene were equilibrated together show consistent partitioning, with $D^{ol/cpx}>1$ (Fig. 8). A single reversal experiment done at 800 °C (experiment 2m-R), yielded identical results as the forward experiment done at the same conditions. Although the data are somewhat scattered, there does not seem to be any systematic change in $D^{ol/cpx}$ with temperature, which is consistent with observations from mantle peridotites (Seitz and Woodland, 2000). Also shown in Fig. 8 is the ratio of $D_{Li}^{olivine/fluid}/D_{Li}^{cpx/fluid}$ calculated from single-phase experiments, which are consistent with the results from the two-phase experiments. Our determinations of $D^{ol/cpx}$ are also in good agreement with the value of ~2 measured by Ottolini et al. (2009) from coexisting phases in mineral–melt partitioning experiments done at 1 GPa and 1330 °C.

4.4. Experiments at variable fO_2

Three experiments were conducted to investigate $D_{Li}^{ol/cpx}$ as a function of Fo content of olivine. Experiment 2m-lo was run at 1000 °C in a Pt lined Mo capsule (FMQ − 4.4) resulting in a $D_{Li}^{ol/cpx}$ of 0.7. Experiment 2m-3 was run in a standard Ni lined Pt capsule at 1000 °C (FMQ − 0.4) and resulted in a $D_{Li}^{ol/cpx}$ of 4.0. Experiment 2m-hi was run at 1000 °C in a Pt lined Re capsule (FMQ + 2.0) resulting in stabilization of only enstatite, which resulted in a $D_{Li}^{en/fluid}$ of 0.02.

4.5. Experiments with added REE

Experiment Yb-1, carried out at 1000 °C with 0.25 mg of Yb_2O_3, was an attempt to determine the effect of rare earth elements (REE) on the relative partitioning of lithium between olivine and clinopyroxene. This experiment resulted in olivine with 175 ppm lithium and clinopyroxene with 17 ppm lithium, and a $D^{ol/cpx}{}_{Li}$ of 10. This value is significantly higher than the $D^{ol/cpx}{}_{Li}$ of 4.0 at 1000 °C that results from no addition of REE. The increased partitioning of lithium into the olivine is consistent with a coupled substitution with Yb^{3+}.

4.6. Lithium isotope fractionation

4.6.1. Clinopyroxene-fluid

Table 6 gives the isotopic ratios of the starting materials and run products from the isotopic fractionation experiments as well as the calculated $\Delta^7Li_{cpx-fluid}$, where;

$$\Delta^7Li_{cpx-fluid} = \delta^7Li_{cpx}(‰) - \delta^7Li_{fluid}(‰). \quad (5)$$

Duplicate experiments at 900 °C and run times of 72 and 142 h had $\Delta^7Li_{cpx-fluid}$ within ±2‰, within the precision of the analysis,

Table 6
Isotopic composition of starting materials and run products.

Exp	T (°C)	Starting material		Products		$\Delta^7Li_{cpx-fluid}$ (‰)	$\Delta^7Li_{ol-fluid}$ (‰)	Δ^7Li_{ol-cpx} (‰)
		fluid δ^7Li (‰)	mineral δ^7Li (‰)	mineral δ^7Li (‰)	2 s[a] (‰)			
MC-ICPMS data (UMD)								
Cpx–fluid experiments using ^{6}Li doped solution								
LDi-10	900	−88	+10	−91	1	−3		
LDi-11	900	−88	+10	−91	1	−3		
LDi-12*	900	−46	−91	−50	1	−3		
LDi-15	900	−88	+10	−89	1	−1		
LDi-17	1000	−88	+10	−90	1	−1		
LDi-18	1100	−88	+10	−89	1	0		
Cpx–fluid experiments using LSVEC solution								
NCDL-6	900	0	+10	−3	1	−3		
SIMS data (LLNL)								
Cpx–fluid experiments using LSVEC solution								
NCDL-2	800	0	+10	−2	4	−2		
NCDL-4	1000	0	+10	−1	4	−1		
NCDL-5	1100	0	+10	−3	4	−3		
NCDL-6	900	0	+10	−4	4	−4		
Olivine-cpx experiments using LSVEC solution								
Clinopyroxene								
2m-2 cpx	800	0	+10	−4	4			
2m-3 cpx	1000	0	+10	−7	4			
2m-R cpx*	800	−3	−4	−4	4			
Olivine								
2m-2 ol	800	0	+1	+2	4			+6
2m-3 ol	1000	0	+1	−1	4			+6
2m-R ol*	800	−3	+2	−8	4			−3
2m-R mtc*	800	−3	+1	−15	4			

* denotes reversal experiment.
[a] 2 s refers to 2 sigma error based on the precision of the measurement.

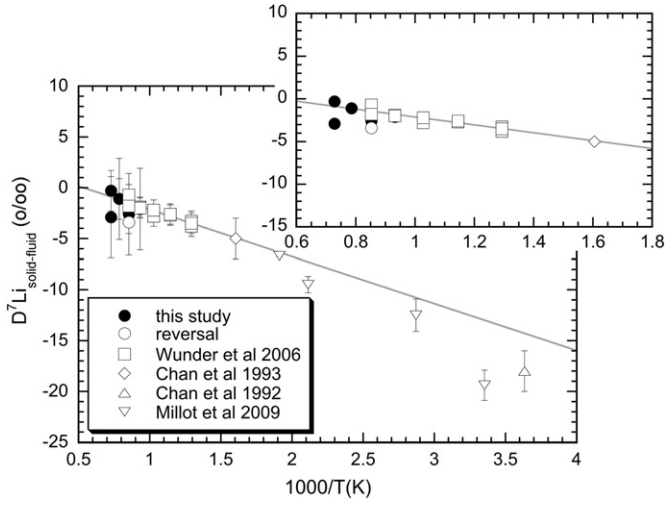

Fig. 9. Mineral/fluid isotopic fractionation of lithium. $\Delta^7Li_{cpx-fluid}$ (‰) as a function of 1000/T (K). The results are shown from this study, the spodumene-fluid experiments of Wunder et al. (2006), the basalt-seawater experiments of Millot et al. (2009) and the basalt-seawater measurements of Chan et al. (1993; 350 °C) and Chan et al. (1992; 2 °C). Also shown is the regression line constrained by the experiments of Wunder et al. (2006). Error bars for this study are 2σ, based on counting statistics of the analyses.

indicating that run times were sufficient for isotopic equilibrium. A reversal experiment, Ldi-12, equilibrated a split of sample Ldi-10 (δ^7Li of −91‰) with solution B (δ^7Li −46‰), and resulted in a $\Delta^7Li_{cpx-fluid}$ of -3 ± 2‰, within the precision of the other experiments. The range of $\Delta^7Li_{cpx-fluid}$ measured in this study is from 0 ± 2‰ to -3 ± 2‰, and follows the trend of $\Delta^7Li_{cpx-fluid}$ decreasing with increasing temperature described by the experiments of Wunder et al. (2006) and measurements of Chan et al. (1992, 1993). When the run products were not rinsed prior to sample digestion and analysis, the data produced scattered results, most likely due to the precipitation of lithium as the remainder of the solution was dried down after sample recovery.

Fig. 9 is a plot of the $\Delta^7Li_{cpx-fluid}$ (‰) versus 1000/TK with data from this study, as well as the $\Delta^7Li_{spodumene-fluid}$ (‰) from Wunder et al. (2006) and the $\Delta^7Li_{basalt-fluid}$ (‰) measured between basalt and seawater at 350 °C (Chan et al., 1993) and 2 °C (Chan et al., 1992). Wunder et al. (2006) used both OH- and Cl-bearing fluids, whereas fluids in this study are chlorine free, with the lithium introduced as Li_2CO_3. Nonetheless, all of the data plot on the same regression line empirically determined by Wunder et al. (2006). There appears to be no difference in fractionation behavior with pressure (seafloor to 2 GPa) or complexing anion.

Measurements of lithium isotopic fractionation in the quartz–muscovite–fluid system, determined from 400 to 500 °C, found the solids (quartz and mica) to be preferentially enriched in ^{7}Li (Lynton et al., 2005). Such a result is inconsistent with this and previous studies, which showed preferential enrichment of ^{7}Li in the fluid.

4.6.2. Olivine–clinopyroxene lithium isotope fractionation

Table 6 gives the isotopic ratios of the starting materials, run products, and the calculated Δ^7Li_{ol-cpx}, where;

$$\Delta^7Li_{ol-cpx} = \delta^7Li_{ol}(‰) - \delta^7Li_{cpx}(‰). \quad (6)$$

All experiments, with the exception of the reversal runs, had 82 wt.% Dekalb diopside + 18 wt.% San Carlos olivine as starting material. The isotopic composition of the olivine grains, (δ^7Li = +1‰) was coincidentally in isotopic equilibrium with the fluid added and therefore did not shift significantly; whereas, the isotopic composition of the clinopyroxene became as much as 15‰ lighter (i.e. from δ^7Li of +10‰ to −4‰). Δ^7Li_{ol-cpx} measured in this study is $+6\pm6$‰, which is not resolvable with the precision of this study.

5. Discussion

5.1. Controls on partitioning

5.1.1. Clinopyroxene

Clinopyroxene has two cation sites, M1 and M2; M1 has six-fold coordination with respect to oxygen and M2 has eight-fold coordination. Given that the M1 site is slightly smaller than M2 (optimal site radius (r_o) of ~0.7 Å versus M2 r_o of ~1.1 Å) and has lower defect energies for univalent cations, it is likely that the primary site for lithium in the clinopyroxene structure is M1 where it can exchange for Mg^{2+} (Purton et al., 1997). Such an exchange should be coupled by a trivalent cation such as Al^{3+} in jadeite ($NaAlSi_2O_6$) component or spodumene ($LiAlSi_2O_6$) or Fe^{3+} in an aegirine-like molecule, $NaFe^{3+}Si_2O_6$, according to the following exchange reaction:

$$Li^{1+} + X^{3+} \Leftrightarrow \left(Mg^{2+}\right)_{M1} + \left(Ca^{2+}\right)_{M2}. \quad (7)$$

Previous work has shown lithium partitioning between clinopyroxene and aqueous fluids increases slightly with increasing Al/Si ratio (Brenan et al., 1998b). The results of this study are consistent with those findings (Fig. 5). The run product clinopyroxene from the clinopyroxene/melt experiment of Blundy and Dalton (2000) at 1375 °C (and 0.8 GPa) has a similarly low alumina content as the clinopyroxene from this study, and plots on the Arrhenius regression line determined in this study. As the alumina content of the clinopyroxene increases, lithium partitioning increases and the partition coefficient falls above the regression line. This relationship is consistent with Eq. (7) where lithium substitution is coupled with Al^{3+}. Other elements, such as Fe and Na, appear to influence the lithium partitioning as well. Fe in trivalent form should enhance the uptake of lithium in a similar coupled substitution as described in Eq. (7). However the addition of divalent cations such as Na would have the opposite effect as lithium would not be charge balanced when coupling with a divalent cation and such a $Li^+ + X^{2+}$ substitution would not be preferred. For example, the experiment of Brenan et al. (1998b) labeled 1.5* was conducted with 0.5 M aq NaCl, and despite resulting in a run product clinopyroxene with 1.5 wt.% Al_2O_3 and 0.25 wt.% Na_2O resulted in a lower clinopyroxene/fluid partition coefficient than measured in another experiment from that study containing 0.2 wt.% Al_2O_3 and 0.03 wt.% Na_2O (Brenan et al., 1995) and the experiment containing 0.3 wt.% Al_2O_3 and 0.02 wt.% Na_2O from this study.

5.1.2. Olivine

Previous studies have shown lithium partitioning between olivine and silicate melt to be coupled with Al^{3+} (Suzuki and Akaogi, 1995; Taura et al., 1998). This is consistent with the calculations of Purton et al. (1997) which have demonstrated that the most favorable mechanism for substitution of a univalent cation in forsterite involves pairing a 3^+ cation in the M2 site with a 1^+ cation in the M1 site. Such observations suggest the following mechanism for incorporating lithium into olivine:

$$Li^{1+} + X^{3+} \Leftrightarrow \left(Mg^{2+}, Fe^{2+}\right)_{M1} + \left(Mg^{2+}, Fe^{2+}\right)_{M2}. \quad (8)$$

In Fig. 6, the temperature-dependence of the partition coefficients measured from the olivine-fluid experiments of this study is compared to the olivine-melt experiments from previous studies (Brenan et al., 1998a; Taura et al., 1998; Blundy and Dalton, 2000; Zanetti et al., 2004; Ottolini et al., 2009; Grant and Wood, 2010). The data points are labeled with the wt.% FeO in the run product olivine.

The olivine-melt partitioning experiments with low FeO plot on the same regression line as those determined in this study, and lithium partition coefficients increase with increasing FeO in the olivine at a given temperature. Assuming that at a given temperature and fO_2 the total Fe^{3+} content of olivine scales with total Fe content, the trend of increasing lithium partitioning in olivine with increasing FeO, suggests that lithium may be coupling with Fe^{3+} as a substitution mechanism (see Eq. (8)). The data from Zanetti et al. (2004) and Grant and Wood (2010) further support this suggestion. The Zanetti et al. (2004) experiment, labeled 19*, was conducted with a graphite-lined Pt capsule, resulting in fO_2 buffered at FMQ − 2, which is almost three orders of magnitude more reducing than the experimental conditions of this study (FMQ + 0.4). The resulting lithium partition coefficient is much lower than values we have measured, despite the high FeO content of the olivine (19 wt.%). Such reducing conditions would result in lower Fe^{3+} contents, and therefore less favorable conditions for Li^+ substitution, despite the high total FeO content. The Grant and Wood (2010) experiment was conducted with a synthetic Fe-free olivine, which is therefore free of Fe^{3+}, and the lithium partition coefficient plots well below other experimentally determined values.

5.1.3. Plagioclase

The primary control on lithium partitioning between plagioclase and hydrous fluids is the composition of the feldspar (Fig. 7). This is similar to the Sr and Ba partitioning behavior observed between plagioclase and silicate melts or hydrothermal solutions (Blundy and Wood, 1991; Lagache and Dujon, 1987). In the case of Sr or Ba, both these cations are divalent and based on size and charge balance considerations should be accepted more readily into the anorthite structure in exchange for Ca^{2+} rather than Na^+ in the albite structure. This apparent discrepancy is explained by the highly elastic nature of the albite structure (Blundy and Wood, 1991). Albite has a lower bulk modulus and a lower shear modulus than anorthite, which results in an increased "flexibility" of the albite crystal structure (Angel et al., 1988; Blundy and Wood, 1991). These results suggest that the albite crystal lattice would better accommodate Li^+ than the more rigid anorthite structure, despite the fact that Na^+ is larger than Ca^{2+}.

5.1.4. Inter-mineral partitioning

Previous studies of the lithium content in the minerals from mantle xenoliths have found that apparently equilibrated olivine–clinopyroxene pairs (i.e., those that lack chemical inhomogeneities or mineral zoning) tend to fall on a linear correlation between the lithium abundance of the olivine and clinopyroxene (Seitz and Woodland, 2000). Xenoliths apparently metasomatised by silicate melt and/or hydrous fluids fall below the correlation line, and those altered by carbonatite melt fall on and above the correlation. Fig. 10 also includes experimental data corresponding to similar metasomatic regimes, and despite the diversity of compositions produced results have shown $D^{ol/cpx}_{Li} \geq 1$, with the low fO_2 experiment from this study being the exception.

The clinopyroxene compositions resulting from the hydrous fluid experiments from this study have Al_2O_3 contents (0.2–0.3 wt.%) much lower than concentrations in clinopyroxene from mantle xenoliths (2–6 wt.%, Seitz and Woodland, 2000). This might account for high $D^{ol/cpx}_{Li}$ in our experiments, as low Al_2O_3 would result in decreased lithium partitioning between clinopyroxene and fluid. However, experiments in which more aluminous clinopyroxene was equilibrated with olivine in molten carbonate or silicate (Brenan et al., 1998b; Blundy and Dalton, 2000) resulted in $D^{ol/cpx}_{Li} \sim 1$, which is still significantly higher than the hydrous-fluid altered xenoliths.

Given the discrepancy in partitioning between experimentally-equilibrated samples, and the natural xenolith suite, it is possible that the assumption of equilibrium in the some of the natural samples may not be valid. This is consistent with a growing list of studies which have documented disequilibrium inter-mineral partitioning and fractionation of lithium which is attributed to remobilization of lithium, due to infiltration of Li-bearing fluid/melt, with differing rates of diffusion between olivine and clinopyroxene (Parkinson et al., 2007; Rudnick and Ionov, 2007; Jeffcoate et al., 2007; Ionov and Seitz, 2008; Caciagli-Warman, 2010). In many of the natural xenolith samples olivine appears to be depleted in lithium relative to the clinopyroxene. Furthermore, many studies have documented large (~10 ppm) core to rim zoning profiles in clinopyroxene xenoliths and phenocrysts while zoning is of lesser magnitude or absent in coexisting olivine (Rudnick and Ionov, 2007; Parkinson et al., 2007). This has led to the suggestion that lithium diffusion into clinopyroxene is faster than lithium diffusion into olivine, resulting in an increase in the lithium content of clinopyroxene without a corresponding increase the lithium content of the olivine (Rudnick and Ionov, 2007; Parkinson et al., 2007; Ionov and Seitz, 2008; Magna et al., 2008). This is supported by experimentally determined lithium diffusion coefficients in clinopyroxene and olivine which show that lithium diffusion into clinopyroxene is two orders of magnitude faster in clinopyroxene than olivine at similar conditions (Coogan et al., 2005; Caciagli-Warman, 2010; Dohmen et al., 2010).

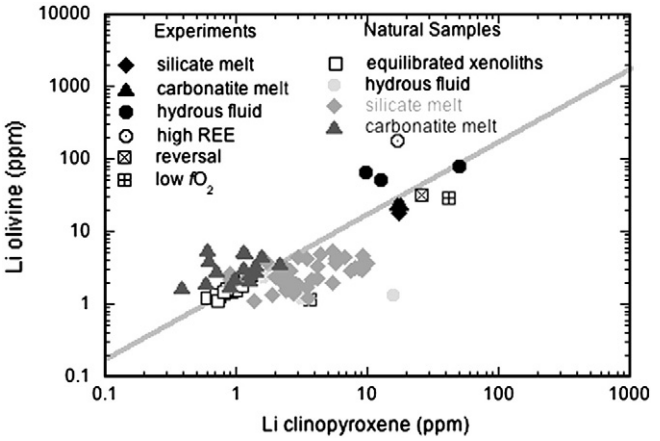

Fig. 10. Lithium partitioning from mantle xenoliths and experimental studies. Lithium abundances in olivine and clinopyroxene from mantle xenoliths (Seitz and Woodland, 2000; Paquin and Altherr, 2002; Woodland et al., 2002, 2004; Aulbach et al., 2008; Magna et al., 2008; Rudnick and Ionov, 2007; Tang et al., 2007) and experimental data (this study, Brenan et al., 1998b; Blundy and Dalton, 2000). Equilibrated olivine–clinopyroxene pairs tend to fall on a linear ~1:1 trend (solid curve), those metasomatised by silicate melts, and hydrous fluids fall below the trend line, and those altered by carbonatite melt fall on and above the trend. The experimental data have higher concentrations of lithium due to experimental and analytical requirements. A silicate melt equilibrated olivine–clinopyroxene pair from Brenan et al. (1998b) plots slightly below the line projected from the equilibrated mantle xenoliths, and carbonatite melt olivine–clinopyroxene pairs from Blundy and Dalton (2000) fall on the projected line, above the silicate melt experiment. Olivine–clinopyroxene pairs equilibrated with hydrous fluids plot well above the values for hydrous fluid metasomatised samples (see text).

5.2. Controls on isotopic fractionation

Lithium isotopic fractionation between minerals and fluids depends on the difference in the zero point potential energy (ZPE) between the phases of interest. ^7Li is heavier and has a lower vibrational frequency, and therefore a lower ZPE than ^6Li (Chacko et al., 2001). The phase that will undergo the greatest reduction in ZPE will preferentially take ^7Li over ^6Li (Chacko et al., 2001). This has been demonstrated by *Ab initio* calculations, which have predicted that during mineral-solution reactions ^6Li is preferentially incorporated into octahedrally coordinated sites in the solid, and ^7Li is preferentially incorporated into the dominantly tetrahedrally coordinated sites in the fluid (Yamaji et al., 2001).

The coordination state and bonding environment of lithium in both spodumene, a clinopyroxene with up to 7% lithium content, and

Ca-clinopyroxene, in this case diopside with 6 to 60 ppm lithium, is octahedral. The consistent fractionation between spodumene and aqueous fluids at 2 GPa (Wunder et al., 2006); clinopyroxene and aqueous fluids at 1 GPa (measured in this study); and altered seafloor basalts (Chan et al., 1992, 1993) suggests that the coordination state of lithium in aqueous fluids does not change throughout this range of conditions.

5.3. The mantle wedge as a chromatograph

The fluids derived from slab dehydration are potentially very rich in lithium, with subducted sediments as a significant source, containing more than 2000 ppm lithium in some cases (Chan et al., 2002). However, consistent and clear correlations of lithium with other fluid mobile elements, such as boron, are rare in arc magmas. It has been suggested that the weak incompatibility of lithium in a mantle mineral assemblage, the rapid diffusion of lithium into mantle minerals, and the high rock/fluid ratio experienced by the fluids in the mantle wedge can provide a mechanism by which the lithium signal is attenuated relative to other fluid mobile trace elements (Tomascak et al., 2000; Tomascak, 2004; Wunder et al., 2006). We evaluate this hypothesis by modeling fluid interaction with the mantle wedge following the method of Navon and Stolper (1987), who considered the mantle as a chromatographic column. In this simple model, the column consists of solid mineral grains with an interconnected fluid network along grain edges. As fluid passes through the column, it achieves instantaneous equilibrium with the coexisting solid. This assumption appears to be justified by the large diffusion coefficients for lithium measured in clinopyroxene and olivine (Coogan et al., 2005; Caciagli-Warman, 2010; Dohmen et al., 2010) implying equilibration time-scales of hours to days at mantle temperatures. With the further assumptions that partition coefficients are constant and the fluid fraction is uniform, the variation in the concentration of a trace element in the fluid (C_f) as a function of time (t) and distance traversed (z) is given by:

$$\frac{\partial C_j}{\partial t} + X_f V_f \frac{\partial C_f}{\partial z} = 0 \tag{9}$$

where X_f is the mass fraction of the trace element in the fluid and V_f is the fluid velocity. It can be shown that the transport velocity of a trace element relative to the transport velocity of the fluid, (V_{tr}/V_{fl}), is equal to the mass fraction of the trace element in the fluid (X_f), which is given by:

$$X_f = \phi\rho_f / (\phi\rho_f + (1-\phi)\rho_s D) \tag{10}$$

where ϕ is the volume fraction of fluid in the column (assumed to be 0.03 by Navon and Stolper, 1987), ρ_f and ρ_s are the fluid density and mantle wedge density; (assumed to be 1 g/cm^3 and 3 g/cm^3 respectively) and, D is the bulk partition coefficient for the element of interest. A notable outcome of Eq. (10) is that V_{tr}/V_{fl} scales with the inverse of the bulk partition coefficient, predicting that there may be a spatial separation between element "fronts," depending on the relative compatibilities of specific elements.

For the case of lithium transport, we use the data in this study, combined with clinopyroxene/orthopyroxene partitioning from Brenan et al. (1998a) to calculate a bulk D for lithium of 0.32, assuming a solid consisting of 60% olivine, 20% orthopyroxene and 20% clinopyroxene. Some petrological models of the mantle wedge predict the presence of chlorite in a zone above the subducted slab (Grove et al., 2009). We expect that this phase will not alter the outcome of the chromatographic model as clinopyroxene/chlorite partition coefficients estimated from natural samples are ~1 (Marschall et al., 2006). We compare results for lithium with those for boron, as arc magmas show clear slab-derived enrichments of this element. The olivine/clinopyroxene, orthopyroxene/melt and clinopyroxene/melt partitioning data for boron from Brenan et al. (1998a) were combined with clinopyroxene/fluid partitioning from Brenan et al. (1998b) to generate a bulk D for boron using the above mineral assemblage. Our calculations show that by the time the fluid has traversed the slab-to-melt source distance, the boron and lithium fronts will have reached 90% and 3% of this distance, respectively, thus strongly decoupling the slab-derived signal for these elements. The maximum capacity of the column for each element can be determined by calculating the time required for the trace element front to reach the top of the column (t), relative to that required for the fluid (t_c), which is given by:

$$\frac{t}{t_c} = \frac{L/X_f V_f}{L/V_f} = \frac{1}{X_f}. \tag{11}$$

For a given column length and a fluid velocity, the boron front will reach the melt source at approximately the same time as the fluid front (1.08 t_c); however, for the lithium front to reach the top of the column requires the column to be filled ~32 times. If lithium transport rates in the mantle are similar to convergence rates, then continuous filling of the column seems unlikely, as the zone of Li-enrichment above the slab will be removed by mechanical coupling between the downgoing slab and overlying mantle. The lithium transport velocity can be estimated by scaling to fluid velocities predicted from U-series disequilibria, which range from 1 to 10 m/year (Elliott et al., 1997; Hawkesworth et al., 1997). Eq. (11) therefore predicts lithium transport velocities of 12 to 120 cm/year (Fig. 11). These overlap, at the lower end, with plate convergence rates of 0.4 to 12 cm/year (Jarrard, 1986), suggesting that the zone of lithium enrichment would be removed from the locus of fluid influx, thus preventing significant migration of the lithium front into the zone of melting.

5.4. Isotopic evolution of slab derived fluids

Interaction of lithium-bearing fluids with mantle minerals will result in changes to the isotopic composition of both phases. If the shift in the isotopic composition of the fluid and the mantle are known, then the amount of fluid: rock interaction can be estimated.

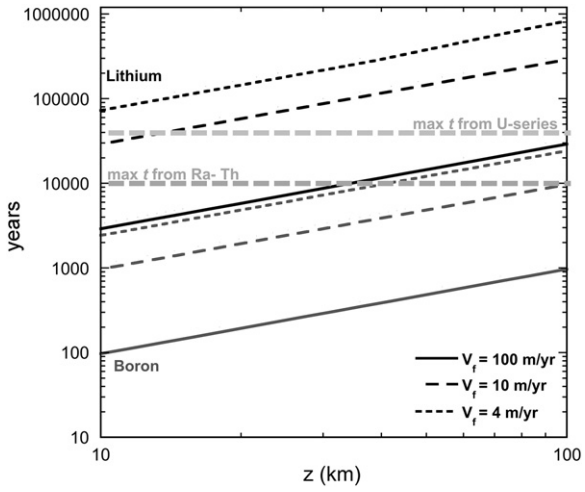

Fig. 11. Time for Li and B transport to top of column. Plot of the time (years) required for an element front to reach the top of a chromatographic column as a function of column height (km) for a fixed column length of 100 km. Time constraints given by U-series and Ra–Th disequilibria are also shown for reference (10,000 to 40,000 years). Because lithium is more compatible in mantle minerals than boron, a lithium signal transported by fluids percolating through the mantle will lag significantly behind the boron signal. The times of transport are calculated from life of the column with respect to each element, in other words; how many times the column can be re-used before its capacity to take up more lithium or boron is reached. The lithium signal will not reach the melt source because it will preferentially partition into the mantle wedge, relative to other fluid mobile elements (such as boron).

Here we apply a simple Rayleigh distillation model to determine what range of isotopic compositions in arc magmas is consistent with fractionation resulting from fluid–rock interaction. In this model, the isotopic composition of the fluid is given by:

$$\delta^7Li_{fluid} = (\delta^7Li_{slabfluid} + 10^3)f^{(\alpha-1)} - 10^3 \quad (12)$$

where δ^7Li_{fluid} is the altered fluid, $\delta^7Li_{slabfluid}$ is the initial composition of the slab-derived fluid, and f is the fraction of the element in the fluid remaining after interaction with the mantle wedge. The magnitude of α is calculated from the relation:

$$\alpha = \left(\delta^7Li_{min} + 1000\right) / \left(\delta^7Li_{fluid} + 1000\right). \quad (13)$$

For the clinopyroxene/fluid partitioning experiments of this study, we calculate a value of α of 0.999 at 1100 °C, which is consistent with the results of Wunder et al. (2006). For lower temperatures, which are more applicable to conditions near the slab-wedge interface (as low as 700–800 °C; Peacock, 1993), values of α will be smaller, and the degree of fractionation larger. To assess this effect, we have also calculated fluid evolution for α of 0.998 and 0.996. Fig. 12 shows how the isotopic composition of a fluid with an initial δ^7Li of +9.7‰, which is the slab input estimated by Moriguti and Nakamura (1998) for the Izu arc, would change during percolation through a mantle column. Because lithium is readily taken up by mantle minerals during this process, the fraction of lithium remaining in the fluid becomes very small, i.e., $X_f \rightarrow 0.03$, and the isotopic composition becomes relatively heavy, with δ^7Li ranging from +15‰ to +35‰ (Fig. 12). Calculated fluid compositions are heavier than the initial slab-derived fluid for any amount of fluid/rock interaction, and become increasingly enriched in ^{7}Li with progressive fluid/rock interaction. This modeling shows that a fluid with an initial δ^7Li of +9.7‰ percolating through the mantle wedge cannot produce magmas with the level of ^{6}Li enrichment found in the Izu arc. Such magmas require sources which have been metasomatised by fluids derived from a ^{6}Li-enriched reservoir.

5.5. Generation of δ^7Li variability in slab derived fluids

The results of this and previous lithium isotope partitioning studies, and theoretical modeling, have demonstrated that during mineral-solution reactions, ^{6}Li is preferentially incorporated into the solid phase (Chacko et al., 2001; Yamaji et al., 2001; Wunder et al., 2006; Chan et al., 1992, 1993). However, recent *ab initio* molecular dynamic (AIMD) calculations by Jahn and Wunder (2009) have determined that at high fluid densities, there may be a shift in the sense of fluid–mineral fractionation, resulting in a preference of ^{6}Li for the fluid phase. This manner of isotopic shift provides a means to generate ^{6}Li-enriched metasomatic fluids, capable of generating isotopically light mantle sources.

Jahn and Wunder (2009) determined that the coordination of lithium in aqueous fluids is mainly 3-fold when fluid densities are less than 1.0 g/cm^3. Because ^{6}Li prefers the higher coordination state, such as 6-fold in most ferromagnesian minerals, ^{7}Li will preferentially partition into the fluid phase at these conditions. However, Jahn and Wunder (2009) also show that as fluid density increases, the coordination of lithium in the fluid also increases. Specifically, when fluid density is greater than 1.2 g/cm^3, the proportion of 5-fold and 6-fold coordinated lithium increases at the expense of the 3- and 4-fold species, so the average lithium coordination in the fluid becomes greater than 4.5. When the lithium coordination in the fluid exceeds that of the solid, the sense of isotopic fractionation changes. Experimental support for this behavior comes from the results of staurolite-fluid partitioning experiments at 3.5 GPa (Wunder et al., 2007) in which staurolite (which contains 4-fold lithium) was found to preferentially incorporate ^{7}Li relative to the fluid phase. To illustrate the conditions at which the sense of partitioning may shift in subduction zone environments, we have calculated fluid densities for Franciscan and Alpine P–T paths using the CORK-EOS (Holland and Powell, 1991) with the Perple_X computer program (Connolly, 2005) and the results are displayed in Fig. 13. Superimposed on this diagram is the calculated average Li-coordination, portrayed as degree of shading. As shown, it is possible to generate ^{6}Li-rich fluids if mineral–

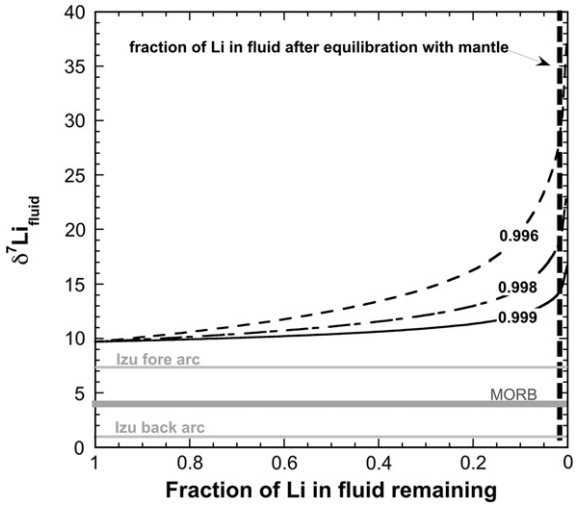

Fig. 12. Evolution of the slab derived fluid by due to Rayleigh distillation. Plot of the evolution of δ^7Li of a fluid percolating through the mantle as a function of fraction of lithium in the fluid remaining. The change in the isotopic composition of a slab-derived fluid with an initial δ^7Li of +10‰ (as estimated for the Izu arc by Moriguti and Nakamura, 1998) during percolation through a mantle column. The isotopic composition of the altered fluid will increase and become heavier than the initial slab derived fluid with any amount of fluid:rock interaction. The mass fraction of Li remaining in the fluid after equilibration with the mantle column is also shown for reference. Because lithium is so readily taken up by the mantle wedge, only a small amount of lithium will remain in the fluid. This will result in extreme fractionation and lead to very ^{7}Li-rich fluids at the top of the melt column. The isotopic composition of both the fore arc and back arc lavas of the Izu arc are shown for reference, as is the δ^7Li of MORB.

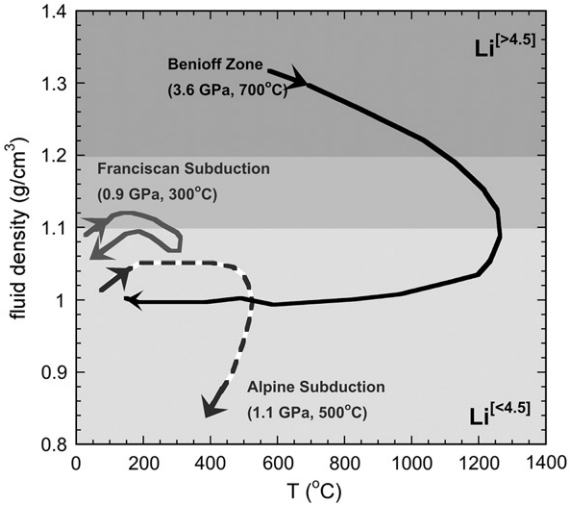

Fig. 13. Lithium coordination and P–T paths. A plot of fluid density as a function of temperature, with the average Li-coordination (from Jahn and Wunder, 2009) shown as degree of shading. Also shown are the fluid densities calculated with the CORK-EOS (Holland and Powell, 1991) using Perple_X program (Connolly, 2005) for Franciscan and Alpine subduction zone P–T paths (from Ernst, 1988) and an ascent path from the slab (Benioff zone) and a fore-arc volcano, ~125 km above the slab (calculated from the thermal model of Peacock, 1993). ^{6}Li-rich fluids will be generated when mineral fluid interaction occurs at depths greater than 125 km, assuming a mantle-slab interface temperature of 700–800 °C. As the fluids percolate up through the mantle wedge and fluid density decreases and the coordination of lithium in the fluids will decrease consequently, ^{6}Li will once again preferentially fractionate into the mineral phase and the fluids will become heavier.

fluid interaction occurs at ~700 °C and depths greater than ~125 km. As fluids percolate up through the mantle wedge, fluid density decreases and the average coordination of lithium in the fluids will decrease; ^{6}Li will once again preferentially fractionate into the mineral phase and the fluids will become isotopically heavier. In order to preserve the ^{6}Li-rich signal generated at depth, fluids need to reach the melt source having undergone minimal interaction with the mantle on their ascent path. Hydrofracture of the mantle by slab-derived fluids is an appealing mechanism to transport lithium through the mantle, as channelized flow through hydrofractures would satisfy the high fluid: rock ratios and rapid fluid velocities required by mineral–fluid partitioning. This transport mechanism would also minimize isotopic fractionation by limiting mineral–fluid interaction, thereby effectively propagating a slab signal all the way to the melt source region.

Lithium in the magmatic suite from Western Anatolia may bear a record of this process. The magma compositions in this region range from calc-alkaline to ultrapotassic and are thought to represent a magmatic sequence initially produced by fluxing of the mantle wedge during subduction, followed by extension and decompression melting (Agostini et al., 2008). Declines of δ^{7}Li and δ^{11}B in both the calc-alkaline and ultrapotassic suites occur in the subduction-related magmas, and track with a deepening of the magma source with decreasing age. Agostini et al. (2008) attribute this ^{6}Li-rich signal to Rayleigh distillation of fluids from the dehydrated slab. However this mechanism is inconsistent with the findings of this study and that of Wunder et al. (2006) which indicates that distillation type reactions would generate ^{7}Li-rich fluids from the dehydrated slab. The low δ^{7}Li in later stage magmas may reflect an increased contribution from deep (>125 km; see Fig. 13) slab-derived fluids generated at pressures where the lithium coordination in the fluid exceeds that of the solid and the sense of isotopic fractionation generates ^{6}Li-rich fluids (Jahn and Wunder, 2009). In order to retain their ^{6}Li-enriched character these fluids must be transported to the melt source region with minimal mantle wedge interaction. Given that the tectonic environment in the Western Anatolian region is becoming extensional coincidental with the generation of the magmas with lowest the δ^{7}Li values (Agostini et al., 2008), fluid transport by hydrofracturing or channelized flow seems a likely mechanism. In such a scenario, the sense of isotopic fractionation in the slab-derived fluid could generate ^{7}Li depleted fluids, which would interact minimally with the overlying mantle wedge, and propagate a light δ^{7}Li signal to the melt source.

6. Conclusions

Our partitioning experiments show that lithium is moderately incompatible in the mantle during mineral–fluid exchange reactions. Data also indicate that the affinity of lithium for mantle solids increases with decreasing temperature, and by the addition of high levels of charge-balancing cations, like Fe^{3+} in olivine and Al^{3+} in clinopyroxene. Application of lithium partitioning data to models of fluid–rock interaction in the mantle wedge reveals that the slab-derived lithium signal is attenuated much more rapidly than other indicators of fluid input, like boron. This result explains the lack of lithium enrichment in arc magmas which otherwise bear evidence for slab inputs to their sources. Consistent with previous work, the sense of isotopic shift between clinopyroxene (and likely other mantle minerals) and fluid is to preferentially incorporate ^{6}Li in the solid, thereby generating isotopically heavy fluids. Simple Rayleigh distillation models indicate that, as a consequence of this partitioning, fluid–rock interaction will drive fluid compositions to isotopically heavy values, which cannot explain the variation in isotopic composition of some arc systems (i.e., the Izu arc magmas, Mariana fore arc serpentinites). A possible solution to this inconsistency is changes in the coordination of lithium with increased fluid density, as predicted by the calculations of Jahn and Wunder (2009). Hydrous fluids generated deeper than ~125 km are predicted to contain lithium in coordination states greater than 4-fold, and therefore likely to be enriched in ^{6}Li, at least initially, providing a metasomatic agent capable of generating isotopically light mantle sources.

Acknowledgements

This work was supported by the NSERC Postgraduate Fellowship, Ontario Postgraduate Fellowship and the OGSST J.J. Fawcett Scholarship awarded to N.C and the NSERC equipment and operating funding to J.B. and NSF grant EAR 0609689 to W.F.M. We thank Dr. Ian Hutcheon and Dr. Rick Ryerson for the access to and assistance with the SIMS at LLNL.

Appendix A. Supplementary data

Supplementary data to this article can be found online at doi:10.1016/j.chemgeo.2010.11.025.

References

Agostini, S., Ryan, J.G., Tonarini, S., Innocenti, F., 2008. Drying and dying of a subducted slab: coupled Li and B isotope variations in Western Anatolia Cenozoic Volcanism. Earth and Planetary Science Letters 272, 139–147.

Angel, R.J., Hazen, R.M., McCormick, T.C., Prewitt, C.T., Smyth, J.R., 1988. Comparative compressibility of end-member feldspars. Physics and Chemistry of Minerals 15 (4), 313–318.

Aulbach, S., Rudnick, R.L., McDonough, W.F., 2008. Li–Sr–Nd isotope signatures of the plume and cratonic lithospheric mantle beneath the margin of the rifted Tanzanian craton (Labait). Contributions to Mineralogy and Petrology 155, 79–92.

Ayers, J.C., Brenan, J.B., Watson, E.B., Wark, D.A., Minarik, W.G., 1992. A new capsule technique for hydrothermal experiments using the piston-cylinder apparatus. American Mineralogist 77 (9–10), 1080–1086.

Blundy, J.D., Wood, B.J., 1991. Crystal-chemical controls on the partitioning of Sr and Ba between plagioclase feldspar, silicate melts, and hydrothermal solutions. Geochimica et Cosmochimica Acta 55 (1), 193–209.

Blundy, J.D., Dalton, J., 2000. Experimental comparison of trace element partitioning between clinopyroxene and melt in carbonate and silicate systems, and implications for mantle metasomatism. Contributions to Mineralogy and Petrology 139 (3), 356–371.

Blundy, J.D., Robinson, J.A.C., Wood, B.J., 1998. Heavy REE are compatible in clinopyroxene on the spinel lherzolite solidus. Earth and Planetary Science Letters 160 (3–4), 493–504.

Bouman, C., Elliott, T., Vroon, P.Z., 2004. Lithium inputs to subduction zones. Chemical Geology 212, 59–79.

Boyd, F.R., England, J.L., 1960. Apparatus for phase-equilibrium measurements at pressures up to 50 kilobars and temperatures up to 1750 °C. Journal of Geophysical Research 65 (2), 741–748.

Brenan, J.M., Shaw, H.F., Ryerson, F.J., Phinney, D.L., 1995. Mineral–aqueous fluid partitioning of trace elements at 900 °C and 2.0 GPa: constraints on the trace element chemistry of mantle and deep crustal fluids. Geochimica et Cosmochimica Acta 59 (16), 3331–3350.

Brenan, J.M., Neroda, E., Lundstrom, C.C., Shaw, H.F., Ryerson, F.J., Phinney, D.L., 1998a. Behaviour of boron, beryllium, and lithium during melting and crystallization constraints from mineral–melt partitioning experiments. Geochimica et Cosmochimica Acta 62 (12), 2129–2141.

Brenan, J.M., Ryerson, F.J., Shaw, H.F., 1998b. The role of aqueous fluids in the slab-to-mantle transfer of boron, beryllium, and lithium during subduction experiments and models. Geochimica et Cosmochimica Acta 62 (19–20), 3337–3347.

Caciagli-Warman, N. C., 2010. Experimental Constraints on Lithium Exchange between Clinopyroxene, Olivine and Aqueous Fluid at High Pressures and Temperatures. PhD Thesis. University of Toronto.

Chacko, T., Cole, D.R., Horita, J., 2001. Equilibrium oxygen, hydrogen and carbon isotope fractionation factors applicable to geologic systems. Reviews in Mineralogy and Geochemistry 43 (1), 1–81.

Chan, L.H., Edmond, J.M., Thompson, G., Gillis, K., 1992. Lithium isotopic composition of submarine basalts; implications for the lithium cycle in the oceans. Earth and Planetary Science Letters 108 (1–3), 151–160.

Chan, L.H., Edmond, J.M., Thompson, G., 1993. A lithium isotope study of hot springs and metabasalts from mid-ocean ridge hydrothermal systems; special section on Atlantic hydrothermal activity. Journal of Geophysical Research 98 (B6), 9653–9659.

Chan, L.H., Leeman, W.P., You, C.F., 2002. Lithium isotopic composition of Central American volcanic arc lavas; implications for modification of subarc mantle by slab-derived fluids; correction. Chemical Geology 182 (2–4), 293–300.

Connolly, J.A.D., 2005. Computation of phase equilibria by linear programming: a tool for geodynamic modeling and its application to subduction zone decarbonation. Earth and Planetary Science Letters 236, 524–541.

Coogan, L.A., Kasemann, S.A., Chakraborty, S., 2005. Rates of hydrothermal cooling of new oceanic upper crust derived from lithium-geospeedometry. Earth and Planetary Science Letters 240 (2), 415–424.
Decitre, S., Deloule, E., Reisberg, L., James, R., Agrinier, P., Mével, C., 2002. Behaviour of Li and its isotopes during serpentinization of oceanic peridotites. Geochemistry, Geophysics, Geosystems G3 3 (1).
Deloule, E., Chaussidon, M., Allé, P., 1992. Instrumental limitations for isotope measurements with a Cameca ims-3f ion microprobe: example of H, B, S and Sr. Chemical Geology 101, 187–192.
Dohmen, R., Kasemann, S.A., Coogan, L., Chakraborty, S., 2010. Diffusion of Li in olivine. Part I: experimental observations and a multi species diffusion model. Geochimica et Cosmochimica Acta 74 (1), 274–292.
Eggins, S.M., Rudnick, R.L., McDonough, W.F., 1998. The composition of peridotites and their minerals; a laser-ablation ICP-MS study. Earth and Planetary Science Letters 154 (1–4), 53–71.
Elliott, T., Plank, T., Zindler, A., White, W., Bourdon, B., 1997. Element transport from slab to volcanic front at the Mariana Arc. Journal of Geophysical Research 102 (B7), 14,991–15,019.
Ernst, W.G., 1988. Tectonic history of subduction zones inferred from retrograde blueschist P–T paths. Geology 16 (12), 1081–1084.
Grant, K.J., Wood, B.J., 2010. Experimental study of the incorporation of Li, Sc, Al and other trace elements into olivine. Geochimica et Cosmochimica Acta 74 (8), 2412–2428.
Grove, T.L., Till, C.B., Lev, E., Chatterjee, N., Médard, E., 2009. Kinematic variables and water transport control the formation and location of arc volcanoes. Nature 459, 694–697.
Hart, S.R., Dunn, T., 1993. Experimental cpx/melt partitioning of 24 trace elements. Contributions to Mineralogy and Petrology 113 (1), 1–8.
Hawkesworth, C.J., Turner, S.P., McDermott, F., Peate, D.W., Van Calsteren, P., 1997. U–Th isotopes in arc magmas: implications for element transfer from the subducted crust. Science 276 (5312), 551–555.
Holland, T., Powell, R., 1991. A compensated-Redlich–Kwong (CORK) equation for volumes and fugacities of CO_2 and H_2O in the range 1 bar to 50 kbar and 100–1600 °C. Contributions to Mineralogy and Petrology 109, 265–273.
Holloway, J.R., 1971. Composition of fluid phase solutes in a basalt–H_2O–CO_2 system. Geological Society of America Bulletin 82 (1), 233–237.
Imai, N., Terashima, S., Itoh, S., Ando, A., 1995. 1994 Compilation of analytical data for minor and trace elements in seventeen GJG geochemical reference samples, "Igneous Rock Series". Geostandards Newsletter 19 (2), 135–213.
Ionov, D.A., Seitz, H.M., 2008. Lithium abundances and isotopic compositions in mantle xenoliths from subduction and intra-plate settings: mantle sources vs. eruption histories. Earth and Planetary Science Letters 266, 316–331.
Jahn, S., Wunder, B., 2009. Lithium speciation in aqueous fluid at high P and T studied by *ab initio* molecular dynamics and consequences for Li-isotope fractionation between minerals and fluids. Geochimica et Cosmochimica Acta 73 (18), 5428–5434.
Jarrard, R.D., 1986. Relations among subduction parameters. Reviews of Geophysics 24 (2), 217–284.
Jeffcoate, A.B., Elliott, T., Thomas, A., Bouman, C., 2004. Precise, small sample size determinations of lithium isotopic compositions of geological reference materials and modern seawater by MC-ICP-MS. Geostandards and Geoanalytical Research 28 (1), 161–172.
Jeffcoate, A.B., Elliott, T., Kasemann, S.A., Ionov, D., Cooper, K., Brooker, R., 2007. Li isotope fractionation in peridotites and mafic melts. Geochimica et Cosmochimica Acta 71 (1), 202–218.
Kessel, R., Schmidt, M.W., Ulmer, P., Pettke, T., 2005. Trace element signature of subduction-zone fluids, melts and supercritical liquids at 120–180 km depth. Nature 437 (7059), 724–727.
Lagache, M., Dujon, S.C., 1987. Distribution of strontium between plagioclases and 1 molar aqueous chloride solutions at 600 °C, 1.5 kbar and 750 °C, 2 kbar. Bulletin De Mineralogie 110 (5), 551–561.
Lynton, S.J., Walker, R.J., Candela, P.A., 2005. Lithium isotopes in the system Qz-Ms-fluid: an experimental study. Geochimica et Cosmochimica Acta 69 (13), 3337–3347.
McDonough, W.F., Sun, S., 1995. The composition of the Earth. Chemical Geology 120, 223–253.
Magna, T., Wiechert, U., Halliday, A.N., 2006. New constraints on the lithium isotopic compositions of the Moon and terrestrial planets. Earth and Planetary Science Letters 243 (3–4), 336–353.
Magna, T., Ionov, D.A., Oberli, F., Wiechert, U., 2008. Links between mantle metasomatism and lithium isotopes: evidence from glass-bearing and cryptically metasomatised xenoliths from Mongolia. Earth and Planetary Science Letters 276, 214–222.
Marschall, H.R., Altherr, R., Ludwig, T., Kalt, A., Gméling, K., Kasztovszky, Z., 2006. Partitioning and budget of Li, Be, and B in high-pressure metamorphic rocks. Geochimica et Cosmochimica Acta 70, 4750–4769.
Marschall, H.R., Pogge von Strandmann, P.A.E., Seitz, H.M., Elliott, T., Niu, Y., 2007. The lithium isotopic composition of orogenic eclogites and deep subducted slabs. Earth and Planetary Science Letters 262, 563–580.
Millot, R., Scaillet, B., Sanjuan, B., 2009. Lithium isotopes in island arc geothermal systems: Guadeloupe, Martinique (French West Indies) and experimental approach. Geochimica et Cosmochimica Acta 74 (6), 1852–1871.
Moriguti, T., Nakamura, E., 1998. Across-arc variation of Li isotopes in lavas and implications for crust/mantle recycling at subduction zones. Earth and Planetary Science Letters 163 (1–4), 167–174.
Navon, O., Stolper, E., 1987. Geochemical consequences of melt percolation; the upper mantle as a chromatographic column. Journal of Geology 95 (3), 285–307.
Ottolini, L., Laporte, D., Raffone, N., Devidal, J.L., Le Fevre, B., 2009. New experimental determination of Li and B partition coefficients during upper mantle partial melting. Contributions to Mineralogy and Petrology 157, 313–325.
O'Neill, H.St.C., 1986. Mo–MoO_2 (MOM) oxygen buffer and the free energy of formation of MoO_2. American Mineralogist 71 (7–8), 1007–1010.
O'Neill, H.St.C., 1987a. Quartz–fayalite–iron and quartz–fayalite–magnetite equilibria and the free energy of formation of fayalite (Fe_2SiO_4) and magnetite (Fe_3O_4). American Mineralogist 72 (1–2), 67–75.
O'Neill, H.St.C., 1987b. Free energies of formation of NiO, CoO, Ni_2SiO_4, and CO_2SiO_4. American Mineralogist 72 (3–4), 280–291.
Paquin, J., Altherr, R., 2002. Subduction-related lithium metasomatism during exhumation of the Alpe Arami ultrahigh-pressure garnet peridotite (Central Alps, Switzerland). Contributions to Mineralogy and Petrology 143 (5), 623–640.
Parkinson, I.J., Hammond, S.J., James, R.H., Rogers, N.W., 2007. High-temperature lithium isotope fractionation; insights from lithium isotope diffusion in magmatic systems. Earth and Planetary Science Letters 257 (3–4), 609–621.
Peacock, S.M., 1993. The importance of blueschist → eclogite dehydration reactions in subducting oceanic crust. Geological Society of America Bulletin 105 (5), 684–694.
Pearce, N.J.G., Perkins, W.T., Westgate, J.A., Gorton, M.P., Jackson, S.E., Neal, C.R., Chenery, S.P., 1997. A compilation of new and published major and trace element data for NIST SRM 610 and NIST SRM 612 glass reference materials. Geostandards Newsletter 21 (1), 115–144.
Pownceby, M.I., O'Neill, H.St.C., 1994. Thermodynamic data from redox reactions at high temperatures; IV, calibration of the Re–ReO_2 oxygen buffer from EMF and NiO + Ni–Pd redox sensor measurements. Contributions to Mineralogy and Petrology 118 (2), 130–136.
Purton, J.A., Allan, N.L., Blundy, J.D., 1997. Calculated solution energies of heterovalent cations in forsterite and diopside; implications for trace element partitioning. Geochimica et Cosmochimica Acta 61 (18), 3927–3936.
Rudnick, R.L., Ionov, D.A., 2007. Lithium elemental and isotopic disequilibrium in minerals from peridotite xenoliths from Far East Russia: product of recent melt/fluid–rock reaction. Earth and Planetary Science Letters 256 (1–2), 278–293.
Ryan, J.G., Langmuir, C.H., 1987. The systematics of lithium abundances in young volcanic rocks. Geochimica et Cosmochimica Acta 51 (6), 1727–1741.
Scambelluri, M., Müntener, O., Ottolini, L., Pettke, T.T., Vannucci, R., 2004. The fate of B, Cl and Li in the subducted oceanic mantle and in the antigorite breakdown fluids. Earth and Planetary Science Letters 222 (1), 217–234.
Seitz, H.M., Woodland, A.B., 2000. The distribution of lithium in peridotitic and pyroxenitic mantle lithologies; an indicator of magmatic and metasomatic processes. Chemical Geology 166 (1–2), 47–64.
Seyfried Jr., W.E., Chen, X., Chan, L.H., 1998. Trace element mobility and lithium isotope exchange during hydrothermal alteration of seafoor weathered basalt: an experimental study at 350 °C, 500 bars. Geochimica et Cosmochimica Acta 62 (6), 949–960.
Suzuki, T., Akaogi, M., 1995. Element partitioning between olivine and silicate melt under high pressure. Physics and Chemistry of Minerals 22 (7), 411–418.
Tang, Y.J., Zhang, H.F., Nakamura, E., Moriguti, T., Kobayashi, K., Ying, J.F., 2007. Lithium isotopic systematics of peridotite xenoliths from Hannuoba, North China Craton: implications for melt–rock interaction in the considerably thinned lithospheric mantle. Geochimica et Cosmochimica Acta 71, 4327–4341.
Taura, H., Yurimoto, H., Kurita, K., Sueno, S., 1998. Pressure dependence on partition coefficients for trace elements between olivine and the coexisting melts. Physics and Chemistry of Minerals 25 (7), 469–484.
Teng, F.Z., McDonough, W.F., Rudnick, R.L., Dalpé, C., Tomascak, P.B., Chappell, B.W., Gao, S., 2004. Lithium isotopic composition and concentration of the upper continental crust. Geochimica et Cosmochimica Acta 68 (20), 4167–4178.
Tomascak, P.B., 2004. Developments in the understanding and application of lithium isotopes in the earth and planetary sciences; geochemistry of non-traditional stable isotopes. Reviews in Mineralogy and Geochemistry 55, 153–195.
Tomascak, P.B., Ryan, J.G., Defant, M., 2000. Lithium isotopic evidence for light element decoupling in the Panama subarc mantle. Geology 28 (6), 507–510.
Tomascak, P.B., Widom, E., Benton, L.D., Goldstein, S.L., Ryan, J.G., 2002. The control of lithium budgets in island arcs. Earth and Planetary Science Letters 196 (3–4), 227–238.
Tomascak, P.B., Langmuir, C.H., Le Roux, P.J., Shirey, S.B., 2008. Lithium isotopes in global mid-ocean ridge basalts. Geochimica et Cosmochimica Acta 72 (6), 1626–1637.
Walker, J.A., Teipel, A.P., Ryan, J.G., 2009. Light elements and Li isotopes across the northern portion of the Central American subduction zone. Geochemistry, Geophysics, Geosystems G3 10, Q06S16 (June).
Woodland, A.B., Seitz, H.M., Altherr, R., Marschall, H., Olker, B., Ludwig, T., 2002. Li abundances in eclogite minerals; a clue to crustal or mantle origin? Contributions to Mineralogy and Petrology 143 (5), 587–601.
Woodland, A.B., Seitz, H.M., Yaxley, G.M., 2004. Varying behaviour of Li in metasomatised spinel peridotite xenoliths from western Victoria, Australia; trace element fingerprinting; laboratory studies and petrogenetic processes. Lithos 75 (1–2), 55–66.
Wunder, B., Meixner, A., Romer, R.L., Heinrich, W., 2006. Temperature-dependent isotopic fractionation of lithium between clinopyroxene and high pressure hydrous fluids. Contributions to Mineralogy and Petrology 151 (1), 112–120.
Wunder, B., Meixner, A., Romer, R.L., Feenstra, A., Schettler, G., Heinrich, W., 2007. Lithium isotope fractionation between Li-bearing staurolite, Li-mica and aqueous fluids: an experimental study. Chemical Geology 238 (3–4), 277–290.
Yamaji, K., Makita, Y., Watanabe, H., Sonoda, A., Kanoh, H., Hirotsu, T., Ooi, K., 2001. Theoretical estimation of lithium isotopic reduced partition function ratio for lithium ions in aqueous solution. Journal of Physical Chemistry A 105 (3), 602–613.
Zack, T., Tomascak, P.B., Rudnick, R.L., Dalpé, C., McDonough, W.F., 2003. Extremely light Li in orogenic eclogites: the role of isotopic fractionation during dehydration in subducted oceanic crust. Earth and Planetary Science Letters 208 (279–290).
Zanetti, A., Tiepolo, M., Oberti, R., Vannucci, R., 2004. Trace-element partitioning in olivine: modelling of a complete data set from a synthetic hydrous basanite melt. Lithos 75 (1–2), 39–54.